Macropinocytosis Overcomes Directional Bias in Dendritic Cells Due to Hydraulic Resistance and Facilitates Space Exploration

Hélène Moreau, Carles Blanch-Mercader, Rafaele Attia, Mathieu Maurin, Zahraa Alraies, Doriane Sanseau, Odile Malbec, Maria-Graciela Delgado, Philippe Bousso, Jean-François Joanny, et al.

▶ **To cite this version:**

Hélène Moreau, Carles Blanch-Mercader, Rafaele Attia, Mathieu Maurin, Zahraa Alraies, et al.. Macropinocytosis Overcomes Directional Bias in Dendritic Cells Due to Hydraulic Resistance and Facilitates Space Exploration. Developmental Cell, 2019, 49 (2), pp.171-188.e5. 10.1016/j.devcel.2019.03.024 . hal-02378369

HAL Id: hal-02378369
https://hal.science/hal-02378369

Submitted on 22 Oct 2021

HAL is a multi-disciplinary open access archive for the deposit and dissemination of scientific research documents, whether they are published or not. The documents may come from teaching and research institutions in France or abroad, or from public or private research centers.

L'archive ouverte pluridisciplinaire **HAL**, est destinée au dépôt et à la diffusion de documents scientifiques de niveau recherche, publiés ou non, émanant des établissements d'enseignement et de recherche français ou étrangers, des laboratoires publics ou privés.

Distributed under a Creative Commons Attribution - NonCommercial 4.0 International License

Version of Record: https://www.sciencedirect.com/science/article/pii/S1534580719302357
Manuscript_20f59be040c973d6e678c21d025a3679

Macropinocytosis overcomes directional bias in dendritic cells due to hydraulic resistance and facilitates space exploration

Hélène D. Moreau[1], Carles Blanch-Mercader[2], Rafaele Attia[3,4], Mathieu Maurin[1], Zahraa Alraies[1], Doriane Sanséau[1], Odile Malbec[1], Maria-Graciela Delgado[1], Philippe Bousso[5,6], Jean-François Joanny[2,7], Raphaël Voituriez[8,*], Matthieu Piel[3,4,*] and Ana-Maria Lennon-Duménil[1,*,#]

Affiliations

[1]INSERM U932, Institut Curie, ANR-10-IDEX-0001-02 PSL* and ANR-11-LABX-0043, Paris, France. [2]Laboratoire PhysicoChimie Curie, Institut Curie, PSL Research University - Sorbonne Universités, UPMC – CNRS. Equipe labellisée Ligue Contre le Cancer ; 75005, Paris, France. [3]Institut Curie, PSL Research University, CNRS, UMR 144, F-75005, Paris, France. [4]Institut Pierre-Gilles de Gennes, PSL Research University, F-75005, Paris, France. [5]Institut Pasteur, Dynamics of Immune Responses Unit, 75015 Paris, France. [6]INSERM U1223, 75015 Paris, France. [7]ESPCI Paris-Tech, 10 rue Vauquelin, 75005, Paris, France. [8]Laboratoire Jean Perrin, UM 8237 CNRS/UPMC, 4 place Jussieu, 75005 Paris, France.

* These authors contributed equally to this work.

Lead contact: Ana-Maria Lennon-Duménil.

* To whom correspondence should be addressed: Ana-Maria.Lennon@curie.fr; matthieu.piel@curie.fr; raphael.voituriez@upmc.fr.

© 2019 published by Elsevier. This manuscript is made available under the CC BY NC user license
https://creativecommons.org/licenses/by-nc/4.0/

Summary

The migration of immune cells can be guided by physical cues imposed by the environment such as geometry, rigidity or hydraulic resistance (HR). Neutrophils preferentially follow paths of least HR *in vitro*, a phenomenon known as barotaxis. The mechanisms and physiological relevance of barotaxis remain unclear. We show that barotaxis results from the amplification of a small force imbalance by the actomyosin cytoskeleton, resulting in biased directional choices. In immature dendritic cells (DCs), actomyosin is recruited to the cell front to build macropinosomes. These cells are therefore insensitive to HR, as macropinocytosis allows fluid transport across these cells. This may enhance their space exploration capacity *in vivo*. Conversely, mature DCs down-regulate macropinocytosis and are thus barotactic. Modeling suggests that HR may help guiding these cells to lymph nodes where they initiate immune responses. Hence, DCs can either overcome or capitalize on the physical obstacles they encounter, helping their immune-surveillance function.

Introduction

The immune system is comprised of distinct cell populations that traffic between peripheral tissue and lymphoid organs, continuously surveying their environment for signs of danger. Paramount to a productive immune response is the ability of immune cells to freely patrol all tissues, regardless of the numerous inherent barriers (Heuze et al., 2013). Two important physical constraints that limit immune cell migration are geometrical confinement, which imposes cell and nuclear deformation (Wolf et al., 2013), and hydraulic resistance (HR). HR is a measure of the force needed to move a fluid at a certain speed through a given environment – it thus characterizes the resistance that the environment opposes to fluid displacement. It depends on geometrical parameters and fluid viscosity, and constitutes an intrinsic property of the tissue. HR can oppose a force to cell motion because it restrains the fluid that cells displace as they move. While the impediment to cell migration due to cell and nucleus deformation has been extensively studied (Denais et al., 2016; Raab et al., 2016; Rowat et al., 2013; Thiam et al., 2016), the impact of HR is less understood. Recent *in vitro* studies have shown that neutrophil-like HL60 cells preferentially migrate towards low HR paths (Prentice-Mott et al., 2013), suggesting that HR can act as a guidance cue for migrating cells. This phenomenon, referred to as barotaxis, may play an important role in immune-surveillance by impacting immune cell navigation through complex environments. This may be particularly relevant for dendritic cells (DCs), sentinels of the immune system, impacting on their capability to patrol tissues and initiate adaptive immune responses.

It was postulated that barotaxis in HL60 cells may result from active mechanism(s) involving specific receptor(s) and signaling pathway(s) to sense HR (Prentice-Mott et al., 2013). The reason active mechanisms were initially proposed relies on biophysical paradigms of cell motility: traction forces exerted by migrating cells on substratum are

~100-fold higher than forces generated by HR as migrating cells displace the surrounding fluid, suggesting that HR cannot have a direct mechanical effect. However, the range of forces exerted by migrating cells was recently revised by studies showing that adhesion-independent migration of amoeboid-like cells such as DCs (Lammermann et al., 2008) involves forces about a ~100-fold smaller than the traction forces exerted by mesenchymal adhesive cells (Bergert et al., 2015). This result places HR-generated forces in the same range as the propulsive forces exerted by amoeboid-like cells, and suggests that HR forces might directly impact on cell migration without involving specific HR sensing pathways. HR might thus be a substantial resistive force affecting immune cell migration in tissues.

To evaluate the impact of HR on cell migration, we built a single-cell physical model and validated it experimentally. It suggests that HR biases cell migration because it generates a small force imbalance at the scale of the cell, which is amplified by the actomyosin network. This fundamental physical phenomenon most likely applies to a number of situations where amoeboid-like cells encounter resisting external forces as they move. We next investigated the impact of HR on the migration of DCs. Surprisingly, we found that contrary to other amoeboid-like cells, immature DCs (iDCs) are insensitive to HR due to their elevated macropinocytic activity, an intrinsic propensity of iDCs that helps them sampling the environment by continuously ingesting extracellular fluid. Our intravital imaging experiments suggest that the unresponsiveness of iDCs to HR might contribute to their systemic patrolling function. By contrast, mature DCs (mDCs), which down-regulate macropinocytosis, are sensitive to HR-generated forces. Our model suggests that mDCs might benefit from HR guidance by defining the shortest path to lymph nodes, where they initiate adaptive immune responses. Therefore, although HR can represent a physical obstacle for cell migration, our study suggests that DCs can overcome or use this physical constraint to exert their immune-surveillance function.

Results

A theoretical framework for barotaxis

The range of forces that non-adherent cells, e.g. immune cells, migrating under confinement exert on the substratum is comparable to the range of HR forces that they generate by displacing the surrounding fluid (Bergert et al., 2015). We thus hypothesized that barotaxis, the guidance of cells by HR, could result from a purely mechanical interaction between the cell and the surrounding fluid. In other words, cells would preferentially migrate to lower HR paths because these paths provide the least opposition to their migration. To test this hypothesis, we proceeded in three steps: first, establish a minimal cell migration model that includes forces originating from HR; second, run simulations with realistic parameters for cells migrating in the simplest geometry that we could test experimentally, the Y-shaped bifurcation; and third, perform experiments with real cells migrating in Y-shaped devices with controlled HR to compare their barotactic behavior, cell shape and actomyosin dynamics to those predicted by simulations.

We delineated the minimal physical mechanism for barotaxis by identifying the key players and their relative contribution to the process. For this, we built upon a well-established physical model that faithfully reproduces the fast mode of migration of non-adherent cells under confinement (Bergert et al., 2015; Callan-Jones and Voituriez, 2013; Liu et al., 2015; Recho et al., 2014; Recho et al., 2013; Ruprecht et al., 2015). In this model of confined amoeboid cell migration, cells are described as an active poroelastic material, whose constitutive equations stem from the symmetries and conservation laws of the cortical actomyosin system (Joanny et al., 2007; Juelicher et al., 2007; Kruse et al., 2005). The main parameters of the model are: *(i)* the amplitude of the contractile stress, which encodes the interaction between myosin-molecular motors and cortical actin, and

(ii) the cell permeability to the external fluid, which encodes the forces arising as the confined cell passes through the extracellular fluid. The model harbors a simple motility mechanism in confined environments, which is controlled by the level of contractility. Above a critical level, cells exhibit a spontaneous polarization mechanism: random fluctuations of non-polarized cells are amplified, breaking the front-rear symmetry through an accumulation of contractile activity at the rear. This drives spontaneous retrograde flows of the actin cortex, resulting in a net thrust force on the channel walls and therefore a polarized motile state (See **Data S1**).

To investigate the physical mechanisms underlying barotaxis, we extended this model (Callan-Jones and Voituriez, 2013) from a single channel to a three-way bifurcated configuration, with each branch exhibiting variable levels of HR (**Fig. 1A** and **Data S1**). Barotaxis was quantified as the bias in cell migration towards the branch with the least resistance path. When providing a reasonable range for the cell contractility and permeability parameters of the model, simulated cells displayed a directionality bias that increased progressively with HR asymmetry until it reached an upper threshold (**Fig. 1B** and see **Data S1** for model parameterization). This was in agreement with previous experiments highlighting barotaxis (Prentice-Mott et al., 2013). Hence, our physical model is sufficient to recapitulate barotaxis, which can thus be predicted by the mere mechanical interactions between the migrating cell and its environment.

Barotactic behavior of real versus simulated cells

To assess whether our model provides a faithful description of barotaxis, we confronted its predictions with quantitative experimental observations using Y-shaped micro-fabricated channels. The two branches of the 'Y' were engineered to elicit distinct HR forces, with a channel cross section limited to ~20 μm^2 to ensure cell confinement (**Fig. 1C**).

Importantly, HR asymmetry did not induce aberrant channel-wall coating or medium filling (**Fig. S1A**) and cells completely filled the channels (**Fig. S1B**), thus ensuring that HR can produce the expected forces. The bias of HL60 cells and iDCs toward the lower HR path was quantified, as done in cell simulations (**Fig. 1D** and **movie S1**). In accordance with model predictions, we observed a gradual response to HR in both HL60 (**Fig. 1E,** consistent with published data (Prentice-Mott et al., 2013)) and iDCs (**Fig. 1F**), up to a maximal value for dead ends (infinite HR). HL60 cells were slightly more sensitive to low HR increments (for relative HR asymmetry of 5 and 20) as compared to iDCs. Interestingly, when we modified the dead-end bifurcation (DE/1) to increase the HR of the low resistance side (bifurcation DE/20, **Fig. 1C**), we observed a slightly decreased directional bias for iDCs (**Fig. 1E-F**), as predicted by the model (**Fig. 1B**). Overall, the bias decrease was more pronounced in simulated cells, explainable by their range of sensitivity to relative HR asymmetry, which was smaller (from 0 to ~10) than the one of real cells (from 0 to >20). In other words, the migration bias of simulated cells had already plateaued at relative HR asymmetry of 20. Therefore, simulated cells did not respond strongly to HR differences between DE and 20, whereas they were highly sensitive to HR differences between DE and 3 as well as DE and 10 (**Fig. S1C** and **Data S1**). Therefore, both real and simulated cells display a gradual response to HR with a sensitivity that depends on absolute HR values.

A key requirement for our barotaxis model to apply is that confined cells use an adhesion-independent migration mode that relies on the exertion of minimal forces on their environment. In agreement with previous findings, we found that iDC velocity only slightly decreased in PEG-coated microchannels (**Fig. S1D**) (Lammermann et al., 2008; Renkawitz et al., 2009), showing that they use a non-adhesive migration mode. iDCs also remained barotactic in these low-friction conditions (**Fig. S1E**). Of note, the model

predicted both the decreases in migration speed and bias (**Fig. S1F, G**). Our experimental observations are therefore consistent with the theory: barotaxis can simply result from a mechanical process in which cells choose the path opposing the least resistance to their migration.

A small force imbalance amplified by the actomyosin network accounts for barotaxis

To determine to which extent the conclusions drawn from our model are applicable to the mechanisms that drive barotaxis in real cells, we compared the main model ingredient, actomyosin dynamics, to experimental observations. Using a previously described method to generate actin density maps (Vargas et al., 2016), we confirmed that actin and myosin II accumulated at the rear of iDCs, similar to simulated cells (**Fig. 2A**). Particle instantaneous velocity (PIV) analysis (**movie S2**) showed the expected retrograde actomyosin flow at the rear of both simulated and real cells (**Fig. 2B,** see also kymograph analysis in **Fig. S2A**). Of note, myosin II flow could not be measured at the leading edge of iDCs, as the amount of myosin II was under the levels of detection at this particular subcellular localization. These results show that the migration mechanism on which the model is built is consistent with the actomyosin dynamics observed in iDCs.

To test whether our model could be used to understand the mechanism by which cells choose low HR paths, we quantified the morphological changes that simulated (**Fig. 2C** and **movie S3A**) and real cells (**Fig. 2D** and **movie S3A**) undergo when crossing symmetric (HR relative asymmetry of 1 in Fig. 1C) and asymmetric Y-shaped bifurcations (DE/1 in Fig. 1C). For simulated cells, in both types of bifurcation, we observed that: *(i)* cells form two symmetric arms (one per outlet) that extend at the same speed, *(ii)* the subsystem constituted by these two arms eventually reaches a critical size at which one of the arms decelerates, and *(iii)* retracts (**Fig. 2C and 2E)**. The appearance of an asymmetry

between the two arms shortly before the retraction phase suggested the existence of an inherent instability. A similar result was obtained in asymmetric bifurcations implying that the directional bias does not result from HR preventing or slowing down arm extension. Like simulated cells, real cells extended two arms at the same rate until one arm retracted in symmetric as well as asymmetric bifurcations (**Fig. 2D, F** and **S2B**). Thus, in both real and simulated cells, the HR difference biases the instability arising in the extending arms, resulting in barotaxis.

Because real cells behaved similarly to simulated cells, we revisited the simulation approach to better understand the origin of the instability and bias imposed by HR. In simulated cells in straight channels, the dynamic instability of the actomyosin cytoskeleton resulted in spontaneous polarization (**Fig 2A-B** and **Data S1**). In Y-shaped bifurcations, the subsystem constituted by the two upper extending arms can be viewed as a cell changing length inside a straight channel. When reaching a critical length, the actomyosin system became unstable, self-polarized and dramatically amplified any infinitesimal difference existing between the extension speed of the two arms. In asymmetric bifurcations, the amplification of the small difference in arm extension speed, typical of systems at criticality in physics, led to a significant barotactic bias towards this path (see **Data S1**). This explains why, although arm length trajectories were similar between symmetric and asymmetric bifurcations (**Fig. 2E**), the directional bias increased progressively with HR asymmetry (**Fig 1B**). Our analysis of the model driving the simulated cell behavior thus provides a precise mechanism for barotaxis, based on actomyosin dynamics.

To obtain direct evidence for the role played by the actomyosin system in the directional choice of cells, we quantified the distribution of actin in Y-shaped bifurcations (**movie S3B**). Both simulated and real cells (LifeAct-GFP iDCs) showed a strikingly similar

distribution. In both symmetric and asymmetric cases, we observed no difference in the actin content of the two arms during initial extension (**Fig. 2I** and **S2B**). However, prior to retraction, a localized actin accumulation was detected in only one of the two arms: the arm that ultimately retracted. Strikingly, this accumulation was observed earlier when cells were facing asymmetric bifurcations, compared to symmetric ones (**Fig. 2G,** right for real cells and left for simulated cells). Consistently, GFP-Myosin II (*GFP-Myh9*) also accumulated at the time of retraction in the arm drawing back (**Fig. 2J, S2C, and movie S3C**). The similarities in actomyosin dynamics between the simulated and real cells suggest that the instability of the actomyosin network that drives barotaxis in simulated cells may also apply to real cells. Hence, HR asymmetry strongly biases cell directionality by generating a small difference in resisting forces between the two extending arms, which is further amplified by the actomyosin cytoskeleton. These results indicate that the behavior of the actomyosin network may be sufficient to explain barotaxis.

The polarized distribution of actomyosin is a key determinant for barotaxis

To further investigate this hypothesis, we systematically interrogated the three parameters that control actomyosin dynamics in our model: actin nucleation, depolymerization and contractility. We found that all three factors affected the barotactic behavior of simulated cells (**Fig. 3A**). Pictures of actin distribution in simulated cells showed that, whatever the parameter, highly polarized actin distributions (observed for high contractility, high depolymerization rate and low polymerization input) correlated with higher barotactic bias (**Fig. 3B and S3A**). To confirm these observations, we calculated a polarity index from actin distributions (**Fig. 3C**). We found a strong positive correlation between this polarity index and the barotactic bias, regardless of the actomyosin parameter we modulated (**Fig. 3D**). This constitutes a strong and non-trivial prediction of our model.

To extend these findings to real cells, we capitalized on the heterogeneous actin profiles of iDCs and assessed the correlation between their actin polarity profiles and barotactic bias. Observing single cells and plotting their actin distribution led us to identify three types of profiles (**Fig.3E**): *(i)* strongly polarized (actin accumulated at the rear), *(ii)* poorly polarized ("flat" actin distribution) and *(iii)* symmetric (actin accumulated at both the leading and rear) profiles. To define polarity categories in an objective manner, we calculated the polarity index for individual cells (**Fig. 3C**), ranked them, and placed them into three equal groups: (category 1) the third of the cells with the lowest polarity indexes, (category 2) the third of the cells with intermediate polarity indexes and (category 3) the third of the cells with the highest polarity indexes (**Fig. 3F**). Of note, category 1 regrouped most of the "symmetric" profiles while category 3 regrouped most of the "strongly polarized" profiles. Quantification of the barotactic bias revealed that the more iDCs were polarized, the more they were barotactic (**Fig. 3G**), consistent with the theoretical prediction. Of note, these observations suggest that the various regulators of actomyosin polarity, including the microtubule cytoskeleton, are likely to indirectly impact on the cell barotactic behavior and, more generally, on their ability to rapidly choose between two paths. Because the front-back actin distribution in iDCs is known to strongly depend on myosin-II activity, we next perturbed this distribution using *Myh9*$^{-/-}$ iDCs (Myh9 gene encodes for non-muscle myosin-IIA, the only myosin-II heavy chain isoform expressed in mouse DCs, **Fig. 3H, I**). As predicted, the barotactic bias of these cells was decreased (**Fig. 3J**). This did not result from a change in their size, which was not significantly altered in the absence of myosin II (**Fig. S3B**). Thus, also in real cells, the polarized distribution of the actomyosin cytoskeleton at the time cells reach the bifurcation is a strong determinant for barotaxis, consistent with the non-trivial prediction of our model. We conclude that, in

real cells as in simulated cells, barotaxis results from the amplification of a small force imbalance by an instability of the actomyosin cytoskeleton.

Immature DCs migrating in elevated hydraulic resistance paths are macropinocytic

Having established a mechanism underlying barotaxis that relies on actomyosin dynamics to choose paths of least resistance, we next asked whether some cells may be able to overcome barotaxis and HR to explore dead-ends. Comparison of iDCs migrating in open-ended or dead-ended paths revealed that cells migrating towards dead-ends were slower and actively extended and retracted their leading-edge, where actin accumulated (**Fig. 4A-D, Fig. S4** and **movie S4A**). This was reminiscent of features associated to macropinocytosis, i.e. the ability of iDCs to indiscriminately internalize extracellular fluid, which is essential to their immune sentinel function (Buckley and King, 2017). Macropinocytic iDCs accumulate actomyosin both at the leading edge and rear of the cell (Chabaud et al., 2015; Vargas et al., 2016), resembling the type of actin distribution profile we categorized as 'symmetric' (**Fig. 3E**, left). This subset of cells was belonging to the least barotactic category of cells within the iDC population. These observations suggest a potential correlation between macropinocytosis and barotaxis: the macropinocytic activity of iDCs might allow them choosing dead-end paths more often than non-macropinocytic cells. Notably, comparing cells before and after the bifurcation showed that these features became more pronounced in cells that had passed the bifurcation and migrated towards the dead-end. These observations suggest that macropinocytosis may *(i)* reduce the barotactic bias by helping iDCs to move towards dead-ends, and *(ii)* be further induced in these cells by high HR.

To directly visualize the macropinocytic activity of iDCs, we recorded cells migrating in Y-shaped channels containing fluorescent dextran. We observed that the actin-rich leading

edge of iDCs migrating towards dead-ends (**Fig. 4E**, left panel) formed large fluid-containing vesicles reminiscent of macropinosomes (**Fig. 4E**, middle panel) and eventually transiently flattened (**Fig. 4E**, right panel). Higher resolution imaging confirmed the presence of actin-rich vesicles at the front of iDCs migrating towards dead ends (**Fig. 4F** and **movie S4B**). Accordingly, quantifications of fluorescent Dextran uptake showed that it was significantly higher in iDCs migrating towards dead-ends as compared to cells migrating toward open-ends (**Fig. 4G**). These observations therefore suggest that (1) the few iDCs that chose high HR paths might use macropinocytosis to migrate towards dead-ends, and (2) the macropinocytic capacity of iDCs is enhanced when they migrate towards elevated HR paths as compared to low ones.

Macropinocytosis provides immature DCs with a unique capacity to overcome barotaxis

To explore the link between macropinocytosis and barotaxis, we manipulated the macropinocytic capacity of iDCs by modifying channel geometry. In the narrow channels (cross-section ~20 μm^2) used so far in this study (**Fig. 1-4**), macropinocytosis by iDCs is extremely low, except in the small fraction of cells choosing dead-ends (**Fig. 4)**, explaining the rare occurrence of cells displaying a 'symmetric' actin distribution profile (**Fig. 3E**). We found that the macropinocytic capacity of iDCs was strongly enhanced when we increased the microchannel cross section to ~30 μm^2 (**Fig. 5A, B,** and **movie S5A**), cells remaining nonetheless confined in this larger device (Chabaud et al., 2015). Although the mechanisms accounting for this abrupt change in the macropinocytic rate of iDCs are unknown, we reasoned that we could use this observation to explore the role of macropinocytosis in barotaxis. Macropinocytic iDCs migrating in ~30 μm^2 channels, were no longer sensitive to barotaxis (**Fig. 5C**). Of note, macropinocytosis was also enhanced in iDCs migrating towards dead-ends in ~30 μm^2 micro-channels (**Fig. S5A-D** and **movie S5B**), suggesting that they still faced an increased fluid resistance in dead-ends. In

contrast, HL60 cells, which were not macropinocytic regardless of channel cross section, were barotactic in both ~20 μm^2 and ~30 μm^2 channels, although they were slightly less biased when the cross section increased from ~20 to ~30 μm^2 (**Fig. S5E**). The latter was also observed in simulated cells (see details in **Data S1**) and resulted from decreased HR in microchannels exhibiting a larger cross section (**Fig. S5F**). This decrease in HR having a marginal effect on barotaxis of non-macropinocytic HL60 cells, it cannot explain the complete loss of barotactic bias in macropinocytic iDCs. These results therefore suggest that macropinocytosis endows iDCs with the ability to overcome barotaxis.

To further test this hypothesis, we manipulated the macropinocytic capacity of iDCs. Although there are unfortunately no chemical inhibitors that specifically perturb macropinocytosis alone, we used a number of different strategies that impact on macropinocytosis through targets in different pathways to provide corroborating evidence of the effects of disrupting this cellular process. Pharmacological inhibition of macropinocytosis using EIPA (also known as Amiloride, targets the Nhe1 Na^+/H^+ exchanger) or Rottlerin (targets Protein Kinases C) (Koivusalo et al., 2010; Sarkar et al., 2005; West et al., 1989), restored barotaxis in iDCs migrating in ~30 μm^2 microchannels (**Fig. 5D**). These inhibitors had no impact on barotaxis of iDCs migrating in ~20 μm^2 channels (**Fig. 5D**). Because in ~20 μm^2 channels most iDCs are not macropinocytic, these results suggest that the inhibitors may restore barotaxis by inhibiting macropinocytosis in ~30 μm^2 channels. Equivalent results were obtained when macropinocytosis was genetically compromised by knocking out the gene encoding the Invariant chain *Cd74* (also known as Ii), which recruits Myosin II to the front of iDCs during macropinosome formation (Chabaud et al., 2015). Non-macropinocytic $Cd74^{-/-}$ iDCs were barotactic even in ~30 μm^2 channels (**Fig. 5E**). We further confirmed these findings by indirect inhibition of macropinocytosis (Vargas et al., 2016) using the Arp2/3 inhibitor CK666 (**Fig. S5G**).

Flow cytometry helped us verify that macropinocytosis was indeed inhibited in iDCs under all experimental conditions tested (**Fig. S5H**). Thus, despite the lack of specific tools to manipulate macropinocytosis, our results showing that macropinocytosis and barotaxis are mutually exclusive strongly suggest that macropinocytosis might suppress the bias introduced by HR.

Macropinocytosis reduces barotaxis by facilitating fluid transfer through the cell

According to our model, loss of barotaxis could result from a loss of the small force imbalance that gets amplified by actomyosin instability. We thus hypothesized that macropinocytosis facilitates fluid transfer through the cell, thereby decreasing the opposing force generated by HR. To test this hypothesis, we provided an estimation of the volume of fluid going around or across iDCs migrating in both small and large cross section microchannels filled with fluorescent dextran (**Fig. 5F** and **movie S5C**). Images were segmented to separate internal dextran from external one (red). Internal dextran was further split into leading-edge dextran (green, contained in macropinosomes) and rear dextran (blue, contained in lysosomes as previously described (Chabaud et al., 2015)). For each category, the dextran volume was expressed as the percentage of the channel cross section it occupied. These quantifications showed that the amount of fluid passing through macropinocytic cells migrating in ~30 μm^2 microchannels was strongly enhanced as compared to non-macropinocytic cells migrating in ~20 μm^2 microchannels (15% versus 0% for the fluid contained in macropinosomes, and 25% versus 11% for the fluid between the cell and the channel walls, **Fig. 5F**). Of note, in large channels, we observed that an important portion of external dextran was localized between the cell rear and the channel walls (white star in **Fig. 5F**). Consistent with our previous findings (Chabaud et al., 2015), we observed that in these large channels, iDCs formed macropinosomes at their leading edge and released their fluid content further back on their side, often in the area of the

nucleus (**Fig.5G** and **movie S5D**). This secretion of macropinosomes formed "fluid pockets" around which the cell body deformed as the cell moved forward, resulting in complete translocation of large fluid amounts toward the back of the cell (**Fig.5G** and **movies S5D-E**). These observations suggest that the increased volume between the cell and the channel wall in small channels (~15%) compared to large channels (~24%) actually results for a large part from the release of macropinosomes in the lateral fluid pockets and subsequent cell deformation (~0% in small channels, ~15% in large channels, **Fig. 5F**). These data support a role for macropinocytosis in facilitating fluid transport from the cell front to the cell rear, providing a putative explanation for its effect on barotaxis.

Although macropinocytosis was not part of our initial model, these results show that it has an important impact on the barotactic behavior of macropinocytic iDCs. In our model, total fluid transport through the cell is encoded by the cell-fluid resistance parameter ζ, which comprises passage of fluid on the sides of the cell and through membrane channels as well as through transport by intracellular vesicles. The amount of fluid transport by macropinocytosis can thus be taken into account by modulating this parameter. We quantified barotaxis of simulated cells for different levels of cell permeability (obtained by varying the ratio of cell-fluid resistance and hydraulic resistance ζ/R). We consistently found that cells endowed with a large effective permeability (i.e. "macropinocytic", $\zeta/R=10^{-3}$) are insensitive to barotaxis (bias of 0), while cells exhibiting a small effective permeability (i.e. "non-macropinocytic", $\zeta/R=10^{-1}$) are extremely sensitive to HR asymmetry (**Fig. 5H**). This extended analysis of our model predictions shows that permeability to external fluid is a key parameter for barotaxis, because it modulates the small difference in the resisting force between the two extending arms. Together with our experimental results, they strongly suggest that macropinocytosis can cancel the directional bias introduced by HR, likely by decreasing cell resistance to extracellular fluid (i.e.

increasing cell permeability). Of note, we do not exclude the contribution of other fluid transport mechanisms such as the one involving aquaporins (Stroka et al., 2014) or fluid leakage between the cell and the channel walls (*see discussion*). We conclude that macropinocytic iDCs are insensitive to HR because they transport fluid from their leading edge to their rear.

Macropinocytic immature DCs are more efficient at exploring their environment

We next asked how this effect of macropinocytosis on barotaxis could affect the main function of iDCs, which is tissue patrolling for immunogenic signals. Efficient tissue sampling not only involves large uptake capacity but also productive spatial exploration. We have shown that uptake and migration are coupled via macropinocytosis (Chabaud et al., 2015). This generates a specific type of trajectories in iDCs, corresponding to an intermittent search behavior that could be optimal for sampling of large spaces. However, this study did not take into account the structure and physical properties of the tissue environment, which we here show can strongly bias the migration pattern of iDCs and thus affect spatial exploration. To assess this point *in vitro*, we evaluated at first whether macropinocytic and non-macropinocytic iDCs migrating through channels with HR asymmetries differentially explored the space. Temporal accumulation of single-cell footprints as they migrated through a Y-shaped bifurcation with a dead-end channel showed that macropinocytic cells occupied the whole space evenly, while non-macropinocytic cells left the dead-end part mostly unexplored (**Fig. 6A**). Interestingly, once they have reached the dead-end, most macropinocytic cells reversed their polarity and turned back within a few minutes.

These results prompted us to hypothesize that macropinocytosis might improve the capacity of iDCs to explore tissues in an unbiased manner, allowing them to reach spaces inaccessible to other cells and eventually contributing to their immune sentinel function. Indeed, iDCs

uptake important amounts of external fluid *in vivo*, as observed when injecting fluorescent dextran subcutaneously and analyzing dextran uptake by flow cytometry using surface markers for dermal DCs ($CD45^+$ $CD11c^+$ $MHCII^+$ $EPCAM^-$ cells, **Fig. S6A**). Both the percentage of $dextran^+$ DCs and their dextran mean fluorescence intensity (MFI) increased over time (**Fig. 6B**), showing that dermal DCs internalized extracellular fluid *in vivo*.

To modulate macropinocytosis, we took advantage of *Cd74*-deficient DCs, which show reduced macropinocytosis *in vitro* ((Chabaud et al., 2015; Faure-Andre et al., 2008) and **Fig S5H**). Consistently, we found that $Cd74^{-/-}$ dermal DCs internalized less extracellular fluid than their $Cd74^{+/+}$ counterparts (**Fig. 6C**), indicating that their macropinocytic capacity was reduced *in vivo* as well. To evaluate iDC exploration capacity *in vivo*, we turned to intravital imaging of the mouse ear skin. When CD11c-EYFP endogenous DCs migrated in the dermis, we observed that they constantly extended arms, before retracting one of them to continue their migration (**Fig. 6D** and **movie S6A**). This behavior was reminiscent of the behavior we observed when iDCs faced Y-shaped bifurcations in microchannels (**Fig. 1C** and **2D**), suggesting that they are confronted to similar geometries *in vivo*. Indeed, unlike other amoeboid-like cells such as *Dyctyostelium discoideum* (Bosgraaf and Van Haastert, 2009; Chubb et al., 2002), DCs do not acquire such shape in the absence of physical constrains (**movie S6B)** (see also Renkavitz, 2009).

To address the role of macropinocytosis during tissue exploration, we next generated mixed bone marrow chimeric mice containing both macropinocytic $Cd74^{+/+}$ and low-macropinocytic $Cd74^{-/-}$ iDCs that can be distinguished based on the fluorescent protein (GFP or YFP, respectively) they express. The migration of iDCs in the ear skin was assessed at steady state or after induction of edema by subcutaneous injection of λ-carrageenan (Winter et al., 1962) (**Fig. 6E**), edema being a hallmark of most innate immune responses,. λ-carrageenan injection

induces the typical hallmarks of inflammation (redness, swelling, pain and heat) and triggers prolonged swelling of the inflamed tissue as a result of liquid retention (Morris, 2003; Winter et al., 1962), implying that the fluid cannot flow freely. This suggests that in λ-carrageenan-induced edema, HR is more elevated than in homeostasis. Space exploration by iDCs was quantified as the volume explored by *Cd74*$^{+/+}$ or *Cd74*$^{-/-}$ cells over time using temporal accumulation of single cell footprints from live intravital imaging (**Fig. 6E left, S6B** and **movie S6C**). At steady state, similar volumes were explored by macropinocytic DCs (*Cd74*$^{+/+}$) and non-macropinocytic DCs (*Cd74*$^{-/-}$). In contrast, *Cd74*$^{+/+}$ DCs were significantly more exploratory than their non-macropinocytic *Cd74*$^{-/-}$ counterpart in the presence of edema (**Fig. 6E right**). This was not due to a decrease in their velocity (**Fig. S6C**). Hence, cells permeable to fluid and thus insensitive to HR, such as macropinocytic iDCs, may have an increased capacity to explore inflamed tissues in which the forces needed to displace the fluid are higher. Although to formally conclude on this point, we would need to measure the HR of the direct DC microenvironment *in vivo*, which cannot be easily achieved, this result is consistent with our theoretical and experimental *in vitro* work. It suggests that modulation of barotaxis by macropinocytosis in iDCs might contribute to increase their exploratory capacity, thus favoring tissue patrolling.

Non-macropinocytic mature DCs can use hydraulic resistance as a guidance cue

Our work so far suggests that barotaxis is the result of actomyosin sensitivity to small physical biases in amoeboid-like migrating cells, and that it could be detrimental for the tissue sampling function of iDCs. Macropinocytosis would then counterbalance this detrimental effect by reducing the force imbalance introduced by HR asymmetries present in the migration environment. While tissue sampling and exploration is the main function of iDCs, it is not the case for mature DCs (mDCs), because their function relies on directed

migration towards lymph nodes where they present antigens to T lymphocytes to initiate adaptive immune responses. Maturation of iDCs is induced by danger-associated signals (such as the microbial component LPS). Importantly, macropinocytosis is down-regulated during this maturation process (Sallusto et al., 1995). This suggests that unlike iDCs, mDCs might be sensitive to HR and thus barotactic. To test this hypothesis, we analyzed their migration in asymmetric ~30 μm^2 Y-shaped bifurcations (with one dead-end), which are permissive to macropinocytosis in iDCs. We found that, contrary to iDCs, mDCs preferentially followed low-HR paths (**Fig. 7A**), showing that they were barotactic. To challenge this result, we treated the cells with the formin inhibitor Smifh2, which impairs actin polarization to the cell rear and thus maintains macropinocytosis in mDCs (Vargas et al., 2016). We found that Smifh2-treated mDCs were insensitive to HR asymmetries, like iDCs (**Fig. 7B).** Similar results were obtained when using Cathepsin S (Cts) knocked-out mDCs, which accumulate Myosin II at their leading edge and are highly macropinocytic (Chabaud et al., 2015) (**Fig. 7C**). Of note, under all these experimental conditions, mDCs remained barotactic in ~20 μm^2 channels (**Fig. S7A-C**), consistent with macropinocytosis being highly reduced in cells migrating within such narrow channels (**Fig. 5A, B,** and **movie S8**). Altogether, these results show that the maturation-associated down-regulation of macropinocytosis restores barotaxis in mDCs.

We next asked if barotaxis could play a role in the function of mDCs. After activation, mDCs express the chemokine receptor CCR7, which is essential to guide them to draining lymph nodes. In this context, chemotactic guidance likely plays a dominant role, but physical cues could also impart signs to the cells regarding the shortest path to follow. HR is particularly well suited for this task, as it integrates the resistance over the entire migratory path. This is in contrast to other physical cues, such as geometry and stiffness. Even if cells can respond to such local cues (e.g. through nuclear deformation (Swift et al.,

2013) or focal adhesions (Wang et al., 1993)), they cannot use them to choose the path of global least resistance or the shortest path. Because it is not possible to experimentally dissociate the specific contribution of barotaxis in the long path of cells from peripheral tissues to lymph nodes, we took advantage of our experimentally validated model.

We ran simulations of cells migrating through mazes designed to evaluate whether barotaxis helps them to find the shortest path to a target (**Fig. 7D**). The starting position for the cell in the maze was at the bottom left corner, with the sole exit located in the opposite corner. Simulated cells visited multiple nodes before reaching the exit, and in each case they encountered a Y-shaped bifurcation. Importantly, at each bifurcation, the path of lowest HR was precisely the shortest path to the exit. Two qualitatively different modes of exploration controlled by the ratio ζ/R between cell-fluid resistance and the HR were assayed (See **Data S1**). Highly permeable simulated cells (i.e. weakly barotactic, highly macropinocytic, $\zeta/R=10^{-3}$) chose randomly between both outgoing paths at every node. As a consequence, these cells tended to explore all accessible nodes in the random maze before exiting, performing a purely diffusive motion through the network (**Fig. 7D**, left). Impermeable simulated cells (i.e. strongly barotactic, weakly macropinocytic, $\zeta/R=10^{-1}$) followed the path of least resistance, and therefore, the shortest path to exit among all possible configurations (**Fig. 7D**, right). Explored area (mean area explored over the total network area) and escape time (mean time to exit the maze) were quantified for both types of simulated cells (**Fig. 7E**), showing that for the same random maze, impermeable cells reached the exit faster than permeable cells, whereas permeable cells explored larger regions of maze as compared to impermeable cells. Similar data were obtained for simulation of mazes presenting two exits (**Fig. S7D-F**). These *in silico* results show that non-barotactic cells were the most efficient at fully exploring the network, while barotactic

cells, which selected the path with the least resistance at each node, were able to identify the shortest route across the maze.

Altogether, both our theoretical and experimental results highlight the impact that environmental HR may have on the migratory behavior, and thus, the function of DCs: in iDCs, macropinocytosis minimizes the impact of HR and might thereby facilitate space exploration and tissue patrolling, whereas in mDCs macropinocytosis down-regulation restores barotaxis, which might contribute to their guidance during migration to lymph nodes.

Discussion

In this work, we investigated how the resisting forces that result from the fluid immune cells displace while migrating affect their behavior. We first built a theoretical model that recapitulates the migratory directional bias induced by differences in HR, a phenomenon called barotaxis. By comparing simulated cells generated from the model with immune cells migrating in microchannels of defined geometries, we showed that barotaxis can be explained by a small asymmetry in the resisting forces due to HR, which is amplified by the actomyosin cytoskeleton. Of note, we do not exclude that intracellular pathways regulating actomyosin polarity, such as small GTPases, its regulators (e.g. the microtubule cytoskeleton, acting via regulation of GEF-H1 (Krendel et al., 2002)) and downstream effectors, may have an indirect impact on barotaxis.

Because it is difficult to directly measure the HR-generated forces experienced by migrating cells, we chose to build a theoretical model that takes these forces into account and from which we make predictions that can be experimentally tested. The model can be used to semi-quantitatively reproduce experimental observations without requiring a fine-tuning of all specific parameters. The advantage of this model is that it is detailed enough

to allow precise identification of the physical mechanism responsible for barotaxis. Although we could not experimentally validate all the details of the model ingredients, we were able to test whether non-trivial behaviors of simulated cells, in terms of shape and actomyosin dynamics, were also observed in real cells. This model validation was made possible as we used a well-defined micro-channel geometry, the Y-shaped bifurcation, which resembles the bifurcations DCs face when migrating in fibrous environments *in vivo*. Because HR can be precisely controlled *in vitro* and modulated independently of other parameters, our study constitutes the most unambiguous demonstration that very small forces can strongly bias the directional choice of migrating cells. Importantly, our conclusion does not apply only to HR, but to any environmental cue leading to a force imbalance between the two extending arms of the cell during directional choice. It can thus be extended to a variety of tissue physical properties that introduce biases in the path of migrating cells.

Our experimental data show that macropinocytosis negates barotactic forces on iDCs. However, there are additional mechanisms of fluid transport across cells migrating in microchannels. For example, fluid can pass through the cell membrane by using aquaporins, water-permeable channels that are expressed at the leading-edge of migrating cancer cells (Stroka et al., 2014), or fluid can pass between the cell and channel wall. Of note, EIPA, one of the macropinocytosis inhibitor used in our study, inhibits Nhe1, a sodium/proton pump also involved in water transport across cancer cells (Stroka et al., 2014), stressing the need to ponder the relative contribution of these different water-transport mechanisms to the non-barotactic behavior of iDCs. We believe that macropinocytosis plays a dominant role for several reasons. First, in large channels, macropinocytosis acts as an efficient fluid transfer in iDCs, reaching ~100µm^3/min (estimated from our results (**Fig. 5**) and (Chabaud et al., 2015)), which is about 10 times

more efficient than fluid transfer by Aquaporins/ion pumps (estimated from (Stroka et al., 2014)). Second, pharmacological inhibition of macropinocytosis systematically restores barotaxis, even when using inhibitors that have other molecular targets than the EIPA target Nhe1, such as Rottlerin and CK666. Third, genetic inhibition of macropinocytosis using *Cd74*$^{-/-}$ iDCs (Chabaud et al., 2015) equally restores barotaxis. Thus, although other fluid transfer mechanisms may occur and contribute marginally to the modulation of barotaxis in different cell types, macropinocytosis is the primary process that iDCs exploit to overcome barotactic forces.

We found that iDCs migrating towards dead-ends concentrated actin at their leading edge, and that protrusive activity and macropinocytosis were increased. Two scenarios could be envisioned to explain this result: macropinocytosis induction could result from (1) elevated HR and/or (2) soluble substances secreted by the cells and accumulating in dead-ends. Although we cannot exclude the second possibility, we believe that the first one might be explained by recent studies on the mechanics of branched actin networks. Indeed, a cell migrating in a path with elevated HR experiences higher opposing forces at its leading edge. Such increased mechanical loads have been shown to increase the density of Arp2/3-nucleated branched actin networks (Bieling et al., 2016) and thus the force it exerts on the cell membrane. Because macropinocytosis in iDCs depends on nucleation of branched actin at the leading edge, this physical mechanism could explain macropinocytosis induction by high HR.

Our *in silico* and intravital imaging results suggest that by balancing the ability of DCs to explore their territory versus migrate in a directional manner, macropinocytosis and barotaxis might tune their function as sentinels of the immune system. Importantly, although these *in vivo* experiments validate a prediction of our model and *in vitro* results, they do not directly prove that barotaxis is responsible for the observed phenotypes.

Indeed, while in our model and in the *in vitro* migration device we used to validate it, HR is completely determined by channel geometry, the level of resisting forces that migrating cells experience while displacing fluids in tissues is unknown and challenging to assess. On the same line, we cannot exclude that *in vivo*, CD74 might affect the exploratory behavior of iDCs in the presence of edema by additional means than by decreasing their macropinocytic capacity. This points to the difficulty of assessing the effect of physical variables in complex *in vivo* systems that cannot be experimentally controlled.

Channels of micrometric sizes have been observed within tissues. For example, channels are formed between the connective tissue and the basement membrane of muscles, nerves and epithelia (Friedl and Alexander, 2011). Immune cells are also confined while migrating in blood capillaries in various organs, including the lungs (Yipp et al., 2017). Interstitial spaces also restrict immune cell migration, as they navigate between other cells and collagen fibers (Lammermann and Germain, 2014) but their geometry is more complex. HR, which represents the forces required to move fluid through a given material, is a relevant physiological parameter regardless of the geometry of the tissue environment: the existence of uneven flows of interstitial fluids has been reported (Chary and Jain, 1989), which is a proof that paths exhibiting uneven HR do exist even in interstitial spaces. In the frame of low force amoeboid migration, the forces required to move a cell are of the same order as the forces required to move the surrounding fluid (Bergert et al., 2015). Therefore, the heterogeneities that generate uneven fluid flows *in vivo* are likely to bias cell migration paths as well. Asymmetries in HR could arise for example from heterogeneities in the topological properties of the complex fiber networks. Thus, our results might be relevant for additional contexts of constrained cell migration. Future investigations aimed at characterizing the direct physical environment of immune cells in

tissues should help defining the precise influence of geometry and HR on their migratory behavior *in vivo*.

In conclusion, we here describe how immune cells can overcome and/or capitalize on the physical obstacles such as HR they encounter while exerting their immune-surveillance function in complex environments. We foresee that it may be of particular relevance in the context of anti-tumor immunity, as differences in hydraulic pressure have been reported inside solid tumors (Stylianopoulos et al., 2012; Voutouri et al., 2016).

Acknowledgements

We acknowledge the Cell and Tissue Imaging Facility of the Institut Curie (PICT), a member of the France BioImaging national Infrastructure (ANR-10-INSB-04) and the Curie animal facility. This work has received the support of Institut Pierre-Gilles de Gennes (équipement d'excellence, "Investissements d'avenir", program ANR-10-EQPX-34). We thank C. Hivroz, M. Bretou, D. Obino and K.R. Garrod for insightful comments on the manuscript. We thank Z. Garcia, J. Postat and C. Grandjean from the Bousso lab, as well as J. Helft, M. Heuzé, P. Solanes and J. Pineau for technical help and advice, and C. Goudot for help in statistical analysis. This work was supported by grants from Fondation pour la Recherche Médicale (FRM SPF20140129479) and Association pour la Recherche contre le Cancer (ARC-PDF20140601095) to HDM, the DCBIOL Labex (ANR-10-IDEX-0001-02-PSL and ANR-11-LABX-0043) to AMLD, European Research Council (ERC consolidator grant 311205 PROMICO) to MP, as well as the ANR (PhyMax), the Fondation pour la Recherche Médicale and the Institut National du Cancer to AMLD, MP and RV.

Author contributions

Conceptualization: HDM, CBM, RV, MP, AMLD. Methodology: HDM, CBM, RA, OM, DS, JFJ, RV, MP, AMLD. Investigation: HDM, RA, ZA, CBM, OM, DS. Formal analysis: HDM, CBM, MM, ZA, MGD. Resources: PB. Writing: HDM, CBM, RV, MP, AMLD. Visualization: HDM, CBM, MM. Supervision: RV, MP, AMLD.

Declaration of Interests

The authors declare no competing interests.

References

Bergert, M., Erzberger, A., Desai, R.A., Aspalter, I.M., Oates, A.C., Charras, G., Salbreux, G., and Paluch, E.K. (2015). Force transmission during adhesion-independent migration. Nat Cell Biol *17*, 524-529.

Bieling, P., Li, T.D., Weichsel, J., McGorty, R., Jreij, P., Huang, B., Fletcher, D.A., and Mullins, R.D. (2016). Force Feedback Controls Motor Activity and Mechanical Properties of Self-Assembling Branched Actin Networks. Cell *164*, 115-127.

Bosgraaf, L., and Van Haastert, P.J. (2009). The ordered extension of pseudopodia by amoeboid cells in the absence of external cues. PLoS One *4*, e5253.

Buckley, C.M., and King, J.S. (2017). Drinking problems: mechanisms of macropinosome formation and maturation. FEBS J *284*, 3778-3790.

Callan-Jones, A.C., and Voituriez, R. (2013). Active Gel Model of Amoeboid Cell Motility. New Journal of Physics *15*.

Caton, M.L., Smith-Raska, M.R., and Reizis, B. (2007). Notch-RBP-J signaling controls the homeostasis of CD8- dendritic cells in the spleen. J Exp Med *204*, 1653-1664.

Chabaud, M., Heuze, M.L., Bretou, M., Vargas, P., Maiuri, P., Solanes, P., Maurin, M., Terriac, E., Le Berre, M., Lankar, D.*, et al.* (2015). Cell migration and antigen capture are antagonistic processes coupled by myosin II in dendritic cells. Nat Commun *6*, 7526.

Chary, S.R., and Jain, R.K. (1989). Direct measurement of interstitial convection and diffusion of albumin in normal and neoplastic tissues by fluorescence photobleaching. Proc Natl Acad Sci U S A *86*, 5385-5389.

Chubb, J.R., Wilkins, A., Wessels, D.J., Soll, D.R., and Insall, R.H. (2002). Pseudopodium dynamics and rapid cell movement in Dictyostelium Ras pathway mutants. Cell Motil Cytoskeleton *53*, 150-162.

Cross MC, Hohenberg PC (1993) Pattern formation outside of equilibrium. Reviews of modern physics 65: 851.

Denais, C.M., Gilbert, R.M., Isermann, P., McGregor, A.L., te Lindert, M., Weigelin, B., Davidson, P.M., Friedl, P., Wolf, K., and Lammerding, J. (2016). Nuclear envelope rupture and repair during cancer cell migration. Science *352*, 353-358.

Fai TG, Kusters R, Harting J, Rycroft CH, Mahadevan L (2017) Active elastohydrodynamics of vesicles in narrow blind constrictions. Physical Review Fluids 2: 113601.

Faure-Andre, G., Vargas, P., Yuseff, M.I., Heuze, M., Diaz, J., Lankar, D., Steri, V., Manry, J., Hugues, S., Vascotto, F.*, et al.* (2008). Regulation of dendritic cell migration by CD74, the MHC class II-associated invariant chain. Science *322*, 1705-1710.

Filipe-Santos, O., Pescher, P., Breart, B., Lippuner, C., Aebischer, T., Glaichenhaus, N., Spath, G.F., and Bousso, P. (2009). A dynamic map of antigen recognition by CD4 T cells at the site of Leishmania major infection. Cell Host Microbe *6*, 23-33.

Friedl, P., and Alexander, S. (2011). Cancer invasion and the microenvironment: plasticity and reciprocity. Cell *147*, 992-1009.

Gil-Torregrosa, B.C., Lennon-Dumenil, A.M., Kessler, B., Guermonprez, P., Ploegh, H.L., Fruci, D., van Endert, P., and Amigorena, S. (2004). Control of cross-presentation during dendritic cell maturation. Eur J Immunol *34*, 398-407.

Heuze, M.L., Vargas, P., Chabaud, M., Le Berre, M., Liu, Y.J., Collin, O., Solanes, P., Voituriez, R., Piel, M., and Lennon-Dumenil, A.M. (2013). Migration of dendritic cells: physical principles, molecular mechanisms, and functional implications. Immunol Rev *256*, 240-254.

Jacobelli, J., Friedman, R.S., Conti, M.A., Lennon-Dumenil, A.M., Piel, M., Sorensen, C.M., Adelstein, R.S., and Krummel, M.F. (2010). Confinement-optimized three-dimensional T cell

amoeboid motility is modulated via myosin IIA-regulated adhesions. Nat Immunol *11*, 953-961.

Joanny, J.F., Juelicher, F., Kruse, K., and Prost, J. (2007). Hydrodynamic theory for multi-component active polar gels. New Journal of Physics *9*.

Joanny JF, Kruse K, Prost J, Ramaswamy S (2013) The actin cortex as an active wetting layer. Eur Phys J E 36: 52.

Juelicher, F., Kruse, K., Prost, J., and Joanny, J.-F. (2007). Active behavior of the cytoskeleton. Physics Reports *449*, 3-28.

Koivusalo, M., Welch, C., Hayashi, H., Scott, C.C., Kim, M., Alexander, T., Touret, N., Hahn, K.M., and Grinstein, S. (2010). Amiloride inhibits macropinocytosis by lowering submembranous pH and preventing Rac1 and Cdc42 signaling. J Cell Biol *188*, 547-563.

Krendel, M., Zenke, F.T., and Bokoch, G.M. (2002). Nucleotide exchange factor GEF-H1 mediates cross-talk between microtubules and the actin cytoskeleton. Nat Cell Biol *4*, 294-301.

Kruse, K., Joanny, J.F., Juelicher, F., Prost, J., and Sekimoto, K. (2005). Generic theory of active polar gels: a paradigm for cytoskeletal dynamics. The European Physical Journal E *16*, 5-16.

Lammermann, T., Bader, B.L., Monkley, S.J., Worbs, T., Wedlich-Soldner, R., Hirsch, K., Keller, M., Forster, R., Critchley, D.R., Fassler, R.*, et al.* (2008). Rapid leukocyte migration by integrin-independent flowing and squeezing. Nature *453*, 51-55.

Lammermann, T., and Germain, R.N. (2014). The multiple faces of leukocyte interstitial migration. Semin Immunopathol *36*, 227-251.

Lindquist, R.L., Shakhar, G., Dudziak, D., Wardemann, H., Eisenreich, T., Dustin, M.L., and Nussenzweig, M.C. (2004). Visualizing dendritic cell networks in vivo. Nat Immunol *5*, 1243-1250.

Liu, Y.J., Le Berre, M., Lautenschlaeger, F., Maiuri, P., Callan-Jones, A., Heuze, M., Takaki, T., Voituriez, R., and Piel, M. (2015). Confinement and low adhesion induce fast amoeboid migration of slow mesenchymal cells. Cell 160, 659-672.

Marchetti MC, Joanny J, Ramaswamy S, Liverpool T, Prost J, et al. (2013) Hydrodynamics of soft active matter. Reviews of Modern Physics 85: 1143.

Marcy Y, Prost J, Carlier MF, Sykes C (2004) Forces generated during actin-based propulsion: a direct measurement by micromanipulation. Proceedings of the National academy of Sciences of the United States of America 101: 5992–5997.

Millius, A., and Weiner, O.D. (2010). Manipulation of neutrophil-like HL-60 cells for the study of directed cell migration. Methods Mol Biol *591*, 147-158.

Morris, C.J. (2003). Carrageenan-induced paw edema in the rat and mouse. Methods Mol Biol *225*, 115-121.

Muzumdar, M.D., Tasic, B., Miyamichi, K., Li, L., and Luo, L. (2007). A global double-fluorescent Cre reporter mouse. Genesis *45*, 593-605.

Prentice-Mott, H.V., Chang, C.H., Mahadevan, L., Mitchison, T.J., Irimia, D., and Shah, J.V. (2013). Biased migration of confined neutrophil-like cells in asymmetric hydraulic environments. Proc Natl Acad Sci U S A *110*, 21006-21011.

Raab, M., Gentili, M., de Belly, H., Thiam, H.R., Vargas, P., Jimenez, A.J., Lautenschlaeger, F., Voituriez, R., Lennon-Dumenil, A.M., Manel, N.*, et al.* (2016). ESCRT III repairs nuclear envelope ruptures during cell migration to limit DNA damage and cell death. Science *352*, 359-362.

Recho, P., Joanny, J.F., and Truskinovsky, L. (2014). Optimality of Contraction-Driven Crawling. Phys Rev Lett *112*, 218101.

Recho, P., Putelat, T., and Truskinovsky, L. (2013). Contraction-Driven Motility. Phys Rev Lett *111*, 108102.

Renkawitz, J., Schumann, K., Weber, M., Lammermann, T., Pflicke, H., Piel, M., Polleux, J., Spatz, J.P., and Sixt, M. (2009). Adaptive force transmission in amoeboid cell migration. Nat Cell Biol *11*, 1438-1443.

Riedl, J., Flynn, K.C., Raducanu, A., Gartner, F., Beck, G., Bosl, M., Bradke, F., Massberg, S., Aszodi, A., Sixt, M.*, et al.* (2010). Lifeact mice for studying F-actin dynamics. Nat Methods *7*, 168-169.

Rowat, A.C., Jaalouk, D.E., Zwerger, M., Ung, W.L., Eydelnant, I.A., Olins, D.E., Olins, A.L., Herrmann, H., Weitz, D.A., and Lammerding, J. (2013). Nuclear envelope composition determines the ability of neutrophil-type cells to passage through micron-scale constrictions. J Biol Chem *288*, 8610-8618.

Ruprecht, V., Wieser, S., Callan-Jones, A., Smutny, M., Morita, H., Sako, K., Barone, V., Ritsch-Marte, M., Sixt, M., Voituriez, R.*, et al.* (2015). Cortical contractility triggers a stochastic switch to fast amoeboid cell motility. Cell *160*, 673-685.

Sallusto, F., Cella, M., Danieli, C., and Lanzavecchia, A. (1995). Dendritic cells use macropinocytosis and the mannose receptor to concentrate macromolecules in the major histocompatibility complex class II compartment: downregulation by cytokines and bacterial products. J Exp Med *182*, 389-400.

Sarkar, K., Kruhlak, M.J., Erlandsen, S.L., and Shaw, S. (2005). Selective inhibition by rottlerin of macropinocytosis in monocyte-derived dendritic cells. Immunology *116*, 513-524.

Schindelin, J., Arganda-Carreras, I., Frise, E., Kaynig, V., Longair, M., Pietzsch, T., Preibisch, S., Rueden, C., Saalfeld, S., Schmid, B.*, et al.* (2012). Fiji: an open-source platform for biological-image analysis. Nat Methods *9*, 676-682.

Shi, G.P., Villadangos, J.A., Dranoff, G., Small, C., Gu, L., Haley, K.J., Riese, R., Ploegh, H.L., and Chapman, H.A. (1999). Cathepsin S required for normal MHC class II peptide loading and germinal center development. Immunity *10*, 197-206.

Stroka, K.M., Jiang, H., Chen, S.H., Tong, Z., Wirtz, D., Sun, S.X., and Konstantopoulos, K. (2014). Water permeation drives tumor cell migration in confined microenvironments. Cell *157*, 611-623.

Stylianopoulos, T., Martin, J.D., Chauhan, V.P., Jain, S.R., Diop-Frimpong, B., Bardeesy, N., Smith, B.L., Ferrone, C.R., Hornicek, F.J., Boucher, Y.*, et al.* (2012). Causes, consequences, and remedies for growth-induced solid stress in murine and human tumors. Proc Natl Acad Sci U S A *109*, 15101-15108.

Swift, J., Ivanovska, I.L., Buxboim, A., Harada, T., Dingal, P.C., Pinter, J., Pajerowski, J.D., Spinler, K.R., Shin, J.W., Tewari, M.*, et al.* (2013). Nuclear lamin-A scales with tissue stiffness and enhances matrix-directed differentiation. Science *341*, 1240104.

Thiam, H.R., Vargas, P., Carpi, N., Crespo, C.L., Raab, M., Terriac, E., King, M.C., Jacobelli, J., Alberts, A.S., Stradal, T.*, et al.* (2016). Perinuclear Arp2/3-driven actin polymerization enables nuclear deformation to facilitate cell migration through complex environments. Nat Commun *7*, 10997.

Vargas, P., Maiuri, P., Bretou, M., Saez, P.J., Pierobon, P., Maurin, M., Chabaud, M., Lankar, D., Obino, D., Terriac, E.*, et al.* (2016). Innate control of actin nucleation determines two distinct migration behaviours in dendritic cells. Nat Cell Biol *18*, 43-53.

Vargas, P., Terriac, E., Lennon-Dumenil, A.M., and Piel, M. (2014). Study of cell migration in microfabricated channels. J Vis Exp, e51099.

Viville, S., Neefjes, J., Lotteau, V., Dierich, A., Lemeur, M., Ploegh, H., Benoist, C., and Mathis, D. (1993). Mice lacking the MHC class II-associated invariant chain. Cell *72*, 635-648.

Voutouri, C., Polydorou, C., Papageorgis, P., Gkretsi, V., and Stylianopoulos, T. (2016). Hyaluronan-Derived Swelling of Solid Tumors, the Contribution of Collagen and Cancer Cells, and Implications for Cancer Therapy. Neoplasia *18*, 732-741.

Wang, N., Butler, J.P., and Ingber, D.E. (1993). Mechanotransduction across the cell surface and through the cytoskeleton. Science *260*, 1124-1127.

West, M.A., Bretscher, M.S., and Watts, C. (1989). Distinct endocytotic pathways in epidermal growth factor-stimulated human carcinoma A431 cells. J Cell Biol *109*, 2731-2739.

Wilson, K., Lewalle, A., Fritzsche, M., Thorogate, R., Duke, T., and Charras, G. (2013). Mechanisms of leading edge protrusion in interstitial migration. Nat Commun *4*, 2896.

Winter, C.A., Risley, E.A., and Nuss, G.W. (1962). Carrageenin-induced edema in hind paw of the rat as an assay for antiiflammatory drugs. Proc Soc Exp Biol Med *111*, 544-547.

Wolf, K., Te Lindert, M., Krause, M., Alexander, S., Te Riet, J., Willis, A.L., Hoffman, R.M., Figdor, C.G., Weiss, S.J., and Friedl, P. (2013). Physical limits of cell migration: control by ECM space and nuclear deformation and tuning by proteolysis and traction force. J Cell Biol *201*, 1069-1084.

Yipp, B.G., Kim, J.H., Lima, R., Zbytnuik, L.D., Petri, B., Swanlund, N., Ho, M., Szeto, V.G., Tak, T., Koenderman, L.*, et al.* (2017). The Lung is a Host Defense Niche for Immediate Neutrophil-Mediated Vascular Protection. Sci Immunol *2*.

Zhang, Y., Conti, M.A., Malide, D., Dong, F., Wang, A., Shmist, Y.A., Liu, C., Zerfas, P., Daniels, M.P., Chan, C.C.*, et al.* (2012). Mouse models of MYH9-related disease: mutations in nonmuscle myosin II-A. Blood *119*, 238-250.

Figure legends

Figure 1: A theoretical framework for barotaxis. A. Schematic representation of the model. Grey: simulated cell. Orange: surrounding fluid. **B.** Bias of simulated cells is computed as $(N_{LR}-N_{HR})/(N_{LR}+N_{HR})$, where N_{LR} and N_{HR} are the number of cells choosing low and high HR paths, respectively. A value of 0 corresponds to no bias (50% of cells on each path) and of 1 corresponds to full bias (100% of cells choosing the low HR path). The percentage of cells choosing the low HR path is indicated on the right axis. N = 10000 simulations per condition. The parameters are listed in Table S1 (see **Data S1**). **C.** Transmitted light images of microfluidic chips exhibiting different HR on both bifurcation arms. Calculated values of HR relative asymmetry are indicated above each bifurcation. **D.** Ex. of an iDC migrating in a bifurcation ($(R+\Delta R)/R=5$, channel cross-section $<20\ \mu m^2$) and choosing the low resistance path. The cell was highlighted in light orange for clarity. **E.** Bias of HL60 cells towards the low HR path for the bifurcations shown in C. Data are pooled from 5 independent experiments; n = 230, 246, 57, 356, 34. **F.** Bias of iDCs towards the low HR path for the bifurcations shown in C. Data are pooled from 11 independent experiments; n = 254, 291, 157, 478, 60. **Statistics.** All error bars correspond to SEM. Statistics of graph bars show the difference to the value 0 calculated by a binomial test (one-tail p values hypothesis: probability of success > 0.5). Statistical differences between bars were determined by contingency table and Fisher exact test (one-tail p values hypothesis: increasing HR relative asymmetry increases probability of success). **See also Figure S1 and Movie S1.**

Figure 2: A small force imbalance amplified by the actomyosin network explains barotaxis. A. Actomyosin distribution in simulated cells and iDCs. Left: actomyosin density map of simulated cells migrating in channels. Right: Actin (*LifeAct-GFP*) and Myosin-II (*GFP-Myh9*) density maps (generated as described in (Vargas et al., 2016)) of iDCs migrating in channels. Actin: N=4, n=87. Myosin-II: N=2, n=128. The corresponding profiles are shown below. **B.** Actomyosin flow in simulated cells and iDCs. Left: actomyosin flow map of simulated cells migrating in channels. Right: Representative Myosin-II (*GFP-Myh9*) flow of a migrating iDC (before the bifurcation) analyzed by PIV. The corresponding profiles are shown below (for iDCs: mean ± SEM). Negative velocities correspond to retrograde flows. The greyed area is the zone where Myosin-II flow could not be determined in real cells due to insufficient fluorescence signal. **C.** Mask of a simulated cell in a symmetric bifurcation. **D.** Mask of a LifeAct-GFP iDC in a symmetric bifurcation. **E.** Normalized arm length of simulated cells is plotted against normalized time (centered at the retraction time, indicated by the dotted line, see Fig. S2 for normalization). For asymmetric bifurcations, only cells choosing open-ends were pooled. **F.** Average normalized arm length (mean ± SEM) of iDCs is plotted against normalized time (centered at the retraction time, indicated by the dotted line). N=4, n=43 cells / condition. Symmetric bifurcations correspond to the bifurcation "1" and Asymmetric to "DE/1" according to Fig. 1C. **G.** Actomyosin density map of a simulated cell migrating in a symmetric bifurcation. **H.** LifeAct-GFP distribution of an iDC migrating in a symmetric bifurcation. **I.** Average actin ratio (mean ± SEM) between losing and winning arms for simulated cells (left) and iDCs (right) over time (see Fig. S2 for normalization). Retraction time is indicated by dotted lines and grey area. N=4, n=63, 90. For asymmetric bifurcations, only cells choosing open-ends were pooled. Statistics are calculated by a Wilcoxon test as the difference to the theoretical ratio of 1. **J.** Myosin-II accumulates in the losing arm of iDCs. GFP-Myosin II (*GFP-Myh9*) distribution in an iDC migrating in a

symmetric bifurcation. Accumulation in the retracting arm is indicated by the white arrow. The parameters of simulations are listed in Table S1 (see **Data S1**). **Statistics.** ***: p-value < 0.001; *ns*: non significant. **See also Figure S2 and Movies S2 and S3.**

Figure 3: Actomyosin polarity determines barotaxis. A. Bias of simulated cells towards the low HR path in asymmetric (DE/1 in Fig. 1C) bifurcations as a function of relative variations of polymerization source (ϕ_0), depolymerization rate (k_d) and contractility (ϵ). The referential parameters are listed in Table S1 (see SI). N=10000 simulations. **B.** Normalized actin density profiles (corresponding density maps below) of simulated cells as in A. **C.** Method for calculating the polarity index, defined as the difference of actin at the rear half and the front half of the cells normalized to the total cell actin. **D.** Bias of simulated cells towards the low HR path as a function of simulated cell polarity index. N=10000 simulations. Correlation between polarity index and barotactic bias was evaluated by Spearman correlation test: for polymerization source (ϕ_0): r=1, p-value=0.3333; for depolymerization rate (k_d): r=1, p-value=0.0167; for contractility (ϵ): r=1, p-value=0.0028; and for all parameters pooled together: r=0.9702, p-value<0.001. **E.** Ex. of actin profiles (corresponding density map below) for iDCs in channels (before the bifurcation). Polarity indexes are indicated. **F.** Polarity indexes (mean ± SEM) of iDCs for the three categories (cells were classified by increasing polarity indexes and separated in 3 equal groups: category 1 regroups the third of the cells with the lowest polarity indexes, category 3 the third of the cells with the highest polarity indexes and category 2 the third of the cells with intermediate polarity indexes). One dot represents one cell. N=4, n=67 cells per category. **G.** Bias of iDCs towards the low resistance path in asymmetric bifurcations for the three Polarity Index categories. N=4, n=67 cells per category. **H.** Averaged actin profiles of *Myh9*$^{+/+}$ and *Myh9*$^{-/-}$ iDCs. N=2, *n*=61, 53. **I.** Polarity indexes of *Myh9*$^{+/+}$ and *Myh9*$^{-/-}$ iDCs (mean ± sem). One dot represents one cell. N=2, *n*=61, 53. **J.** Bias of *Myh9*$^{+/+}$ and *Myh9*$^{-/-}$ iDCs towards the low HR path in asymmetric

bifurcations. N=4, *n*=253, 199. **Statistics.** All error bars indicate SEM. For polarity indexes (F, I), statistical differences between conditions were determined by a Mann-Whitney non-parametric t-test. For cell bias (G, J), statistics above graph bars indicate difference to the value 0 (corresponding to no bias) calculated by a binomial test (one-tail p values hypothesis: probability of success > 0.5), and statistical differences between bars were determined by contingency table and Fisher exact test (one-tail p values hypothesis: increasing polarity indexes increases probability of success). **See also Figure S3.**

Figure 4: iDCs migrating to dead-ends are macropinocytic. A. Time-lapse images of iDCs migrating in OE or DE. Green: LifeAct, red: Dextran-AlexaFluo647. **B.** Average cell velocity (µm/min, mean ± sem). One dot corresponds to one cell. Statistical analysis was performed using a one-way ANOVA, followed by a Tukey's multiple comparison test. N=4, *n*=73, 75, 20, 25. **C.** Protrusion / retraction activity. Cells were classified as positive if at least one protrusion / retraction of the front was observed in the last 2 min before the bifurcation or during the 3 min after the bifurcation. Percentages of positive (red) and negative (grey) cells are shown. N=4, *n*=128 cells choosing OE, 54 cells choosing DE. **D.** Front actin accumulation. Cells are classified as positive for actin accumulation at their front if actin accumulation is visible at least once in the last 2 min before the bifurcation or during the 3 min after the bifurcations. Percentages of positive (red) and negative (grey) cells are shown. N=4, *n*=128 cells choosing OE, 54 cells choosing DE. **E.** Zoomed images of iDCs migrating in DE. Green: LifeAct. Red: Dextran-AlexaFluor647. White arrowhead: actin protrusion and actin accumulation. White stars: vesicles filled with Dextran. **F.** Confocal image of an iDC migrating in a DE. **G.** Quantification of macropinocytosis for iDCs migrating in OE or DE. One dot corresponds to one cell. Bars indicate the median. Statistical difference between OE and DE groups was determined by Mann-Whitney non-parametric t-test. N=2, *n*=62, 58. **See also Figure S4 and Movie S4.**

Figure 5: Macropinocytosis provides iDCs with a unique capacity to overcome barotaxis. A. iDCs migrating in small (~20 μm^2) or large (~30 μm^2) channels. Green: LifeAct-GFP, red: Dextran-AlexaFluor647. **B.** Quantification of macropinocytosis in small and large channels. One dot represents one cell. Bars correspond to medians. The Mann-Whitney non-parametric t-test was used for statistics. N=2, *n*=43, 34. **C.** Bias towards low resistance path of iDCs migrating in ~20 μm^2 or ~30 μm^2 symmetric (1) or asymmetric (DE/1) bifurcations. N=5, *n*=298, 368, 886, 870. **D.** Bias toward low HR path in ~20 μm^2 or ~30 μm^2 asymmetric bifurcations of iDCs treated or not with EIPA (left, N=3, *n*=153, 135, 220, 261) or Rottlerin (right, N=3, *n*=113, 176, 226, 343). **E.** Bias toward low HR path in ~20 μm^2 or ~30 μm^2 asymmetric bifurcations of *Cd74*$^{-/-}$ iDCs. N=3, n=340, 360, 418, 542. **Statistical analysis of cell bias (C-E).** Statistics above graph bars indicate difference to the value 0 calculated by a binomial test (one-tail p values hypothesis: probability of success > 0.5). Statistical differences between bars were determined by contingency table and Fisher exact test (two-tails p values). **F.** Quantification of fluid passage in ~20 μm^2 or ~30 μm^2 channels around and inside a LifeAct-GFP iDC. 3D reconstruction of Dextran-AlexaFluor647. Dextran signal was segmented as: outside (red, fluid between the cell and the channel walls), inside the half rear (blue, lysosomes), and inside the half front (green, macropinosomes). Percentages correspond to the average percentage of the channel cross-section occupied by Dextran. **G.** Kymograph of an iDC migrating in a ~30 μm^2 channel, forming macropinosomes at the front and releasing their content at the back. 1 image / 15 seconds. Green: LifeAct-GFP, red: Dextran-AlexaFluor647. White arrow indicates one macropinosome whose content is released at the cell rear. Zoomed kymograph (right) of the region indicated on the left. 1 image / 3 seconds. White stars indicate the macropinosome whose content is released between time points 39 and 42. Green dotted line indicates the time at which the macropinosome is released in the extracellular space. The graph below indicates

the average Dextran intensity in a rectangle at the interface between the cell and the channel wall (indicated on the kymograph). The green dotted line shows the time of macropinosome release at which the average intensity between the cell and the channel wall increases due to fluid passage. **H.** Bias of simulated cells towards the low HR path as a function of HR relative asymmetry and for 3 cell-permeability to HR ratios (ζ/R). N = 10000 simulations / condition. Parameters are listed in Table S1 (see **Data S1**). **Statistics.** All error-bars represent SEM. **See also Figure S5 and Movie S5.**

Figure 6: Macropinocytic iDCs better explore their environment. A. Exploration probability of asymmetric bifurcations by macropinocytic (large channels) and non-macropinocytic (small channels) iDCs. N=2, n=48 cells per condition. Graphs were obtained by plotting the profile along a line in the center of the channel on the exploration probability image. Dotted line indicates the position of the bifurcation. **B.** *In vivo* quantification of extracellular fluid uptake by dermal DCs by flow cytometry. Dermal DCs were identified as $CD45^+CD11c^+MHCII^+EPCAM^-$. The % of $Dextran^+$ dermal DCs (mean ± SEM) and the Dextran MFI of $Dextran^+$ dermal DCs (mean ± SEM) are graphed. One dot represents the average value of both injected flanks for one mouse (n=2 mice / condition / experiment). Different symbols are used for different experiments (N=2). A 2-way ANOVA was used for statistics to take into account variability between experiments (p-value for time = 0.0006 for % of $Dextran^+$ dermal DCs and 0.162 for Dextran MFI), followed by Mann-Whitney non-parametric tests for the % of $Dextran^+$ dermal DCs. **C.** *In vivo* quantification of extracellular fluid uptake by $Cd74^{+/+}$ and $Cd74^{-/-}$ dermal DCs by flow cytometry. Analysis was performed as in B. N=2, n=3 mice / condition / experiment. A 2-way ANOVA was used for statistics. **D.** Ex. of migrating $CD11c\text{-}EYFP^+$ DCs imaged by intravital microscopy in the ear dermis. Dotted arrow indicates trajectory, white arrowhead: winning arm, blue arrowhead: losing arm. **E.** Environment exploration by macropinocytic ($Cd74^{+/+}$, magenta) and less-macropinocytic

(*Cd74*$^{-/-}$, cyan) DCs in the ear dermis with or without edema. Exploration images: intravital two-photon image (left), temporal mask of Cd74$^{+/+}$ DCs (threshold on GFP signal, middle), temporal mask of *Cd74*$^{-/-}$ DCs (threshold on YFP signal, right). The volume explored (time projection of temporal masks) normalized to the initial volume ($\Delta V/V_0$) is graphed as a function of time (mean ± SEM). Data were averaged from 4 independent experiments. A two-way ANOVA was used for statistics (p-value for time < 0.001 for both steady state and edema). **See also Figure S6 and Movie S6.**

Figure 7: Non-macropinocytic mature DCs can use HR as a guidance cue. A. Mature DCs (mDCs) are biased in ~30 μm^2 channels. Bias of iDCs and mDCs towards low resistance path in large asymmetric (DE/1 in Fig. 1C) bifurcations. N=3, n=249, 219. **B.** Bias of mDCs towards low HR path in large asymmetric bifurcations, in the presence of Smifh2 or DMSO. N=3, n=138, 162. **C.** Bias towards low HR path in large (>30 μm^2) asymmetric bifurcations of mDCs deficient or not for *Ctss*. N=3, n=115, 364. **A-C.** Statistics above graph bars indicate difference to the value 0 calculated by a binomial test (one-tail p-values hypothesis: probability of success > 0.5). Statistical differences between bars were determined by contingency table and Fisher exact test (two-tails p-values). **D.** Random maze with one exit. Each node represents a three-way bifurcation (see **Data S1**). **E.** Stochastic cell migration in random mazes was simulated for 3 different ratios of cell permeability to HR (ζ/R). Panels show the distribution of paths toward the exit for simulated cells. The color code labels the normalized frequency of visiting a node in the random maze. **F.** Relative area explored and escaping time as a function of the maze size (mean ± SEM). Solid curves show the theoretical predictions for purely diffusive and ballistic migration modes. Simulation parameters are listed in Table S1 (see **Data S1**). N = 10000 simulations / condition. **Statistics.** All error bars indicate SEM. **See also Figure S7.**

STAR METHODS

CONTACT FOR REAGENT AND RESOURCE SHARING

Further information and requests for resources and reagents should be directed to and will be fulfilled by the Lead Contact, Ana-Maria Lennon-Duménil (Ana-Maria.Lennon@curie.fr).

EXPERIMENTAL MODEL AND SUBJECT DETAILS

Cells

Dendritic cells

Bone-marrow derived dendritic cells (DCs) were obtained by culturing bone marrow cells (from both male and female mice) for 10-11 days in complete DC medium (IMDM medium supplemented with fetal calf serum (FCS, 10%), glutamine (20 mM), penicillin-streptomycin (100 U/mL), ß-mercaptoethanol (50 µM) and granulocyte-macrophage colony-stimulating factor (50 ng/mL)- containing supernatant obtained from transfected J558 cells (Gil-Torregrosa et al., 2004)), as previously described (Faure-Andre et al., 2008; Vargas et al., 2014). In brief, bone marrow were collected by flushing of tibias and femurs. Bone marrow cells were put in culture at day 0 in 60 mL of complete DC medium. At day 4, all cells were collected with PBS EDTA (5 mM), spin down and resuspended in fresh complete DC medium at $0.5x10^6$ cells / mL. At day 7, non-adherent cells were removed, semi-adherent and adherent cells were collected with PBS EDTA (5 mM), spin down and resuspended in fresh complete DC medium at $0.5x10^6$ cells / mL. At day 10 or 11, immature DCs (iDCs) were collected by gentle recovery of semi-adherent cells with complete DC medium. Mature DCs were obtained by 30 min treatment of iDCs with lipopolysaccharide (LPS from *Salmonella enterica* serotype typhimurium, 100 ng/mL, Sigma) followed by careful washing (x3) with

complete medium, and used 6-16h post-treatment, as previously described (Vargas et al., 2016).

HL60 cells

The female neutrophil-like human leukaemia HL60 (*actin-GFP* HL60, (Wilson et al., 2013)) cells were cultured in RPMI-Glutamax completed with FCS (10%), penicillin-streptomycin (100 U/mL) and HEPES (25 mM). They were differentiated in neutrophils by adding DMSO Hybri-Max (1.3%, Sigma) to the culture medium for 5-6 days, as previously described (Millius and Weiner, 2010; Thiam et al., 2016).

Mice

C57BL/6J mice were purchased from Charles River. *LifeAct-GFP* (Riedl et al., 2010), *GFP-Myh9* (Zhang et al., 2012), *Cd74*$^{-/-}$ (Viville et al., 1993), *Ctss*$^{-/-}$ (Shi et al., 1999), *Myh9*$^{+/+}$ (*CD11c-Cre*$^{-}$ *Myh9*$^{Flox/Flox}$ (Caton et al., 2007; Chabaud et al., 2015; Jacobelli et al., 2010)), *Myh9*$^{-/-}$ (CD11c-Cre^{+} *Myh9*$^{Flox/Flox}$), *CD11c-EYFP* (Lindquist et al., 2004) *Cd74*$^{-/-}$, *mT/mG* (Muzumdar et al., 2007) and *CD11c-Cre*$^{+}$ *mT/mG*$^{+}$ mice were bred in our SPF animal facilities. Bone marrow was collected from 8-week-old mice to generate DCs as described above. Male and female mice between 6 and 10-weeks of age were used. Bone marrow chimeric mice were generated by lethal γ-irradiation (9 Gy) of *C57BL/6J* or *mT/mG*$^{+}$ recipient male mice, which were reconstituted 2 h later with a mixture of 50% *CD11c-EYFP Cd74*$^{-/-}$ male bone marrow cells and 50% of *CD11c-Cre*$^{+}$ *mT/mG*$^{+}$ *Cd74*$^{+/+}$ male bone marrow cells. The chimeras were let 8-10 weeks to recover before being used for intravital imaging. For these experiments only males were used because they are more resistant to irradiation and long anesthesia for intravital imaging. All animal experiments were performed in accordance to the European and French Regulation for the Protection of Vertebrate Animals used for Experimental and other Scientific purposes (Directive 2010/63; French Decree 2013-118) and

benefited from advices from the Animal Welfare Body of the Institut Curie Research Center and of the Institut Pasteur.

METHOD DETAILS

Theoretical simulations

See Data S1, Physical description of dendritic cell migration at bifurcations.

In vitro migration experiments

Microbifurcation fabrication and imaging

Bifurcations were designed to exhibit different hydraulic resistances (HR) on each side, with a (R+ΔR)/R of 1, 5, 20 or infinite (dead-end). One additional design was made to compare high HR (same design as 20) to infinite HR (dead-end) (See **Fig. 1C**) Two sizes of channels were generated: small channels were 6.5 µm wide and 2.8 µm high (thus had a cross-section of 18 μm^2), large channels were 8.4 µm wide and 3.9 µm high (thus had a cross-section of 33 μm^2). Microchannels were prepared as described previously (Faure-Andre et al., 2008) in polydimethylsiloxane (PDMS RTV 615, from Neyco), coated with Fibronectin (10 µg/mL, Sigma) or PEG (0.1 mg/mL, PLL (20kDa) grafted with PEG (2kDa) from SuSoS Surface technologies) for 1 h and washed with PBS before loading the cells in complete medium. When indicated, Lucifer Yellow (CH, Lithium Salt, 400 µM, from Fisher Scientific), Dextran-AF647 (10,000MW, Anionic, Fixable, 4 mM, from ThermoFisher), EIPA (50 µM, from Sigma), Rottlerin (3 µM, from Santa Cruz), CK666 (25 µM, from Tocris), Smifh2 (25 µM, from Tocris R&D Systems) or DMSO were added to the medium at the indicated concentration. Cells in channels were imaged for 6-12 h using an epifluorescence Nikon TiE video-microscope equipped with a cooled CCD camera (HQ2, Photometrics), using a 10X (NA=0.3) or a 20X (NA=0.75) dry objective. Confocal imaging was performed using a laser

scanning microscope (Leica Dmi8/SP8) equipped with a 20X (NA=0.75) or a 40X (NA=1.35) oil-immersion objective, hybrid detectors and laser diodes (488 nm and 632 nm).

Migration on 2D surfaces

Glass coverslips were coated with Fibronectin (10 µg/mL, Sigma) and washed before adding LifeAct-GFP iDCs in complete medium. Confocal imaging was performed using a laser-scanning microscope (Leica Dmi8/SP8) equipped with a 40X (NA=1.35) oil-immersion objective, hybrid detectors and laser diode (488 nm), one image acquired every minute.

Macropinocytosis assay by flow cytometry

In vitro assay

iDCs were resuspended at 5.10^6 cells/ml in medium, DMSO or indicated inhibitors They were then distributed in 96-well plates by 50µl per well and prewarm15min at 37°C. A control plate was placed on ice. 50µl of AlexaFluor488-labeled ovalbumin (ova-A488, from LifeTechnologies) was added by well at a final concentration of 0.2mg/ml and the cells were incubated for 45 min. Macropinocytosis was stopped by adding 150µl cold PBS. The cells were washed 2 more times in MACS buffer. They were then incubated with 50µl in a mix of Brilliant Violet 510-labeled anti-MHCII (I-A/I-E) (M5/114.15.2, Biolegend) and APC-Cy7-labelled anti-CD115 (AFS98, Biolegen) antibodies for 30min at 0°C. Fluorescence was acquired with a Miltenyi MACSQuant.

In vivo assay

Mice were anesthetized using isoflurane. Dextran-AF647 (10,000MW, Anionic, Fixable, 25µL, 1mg/mL, from ThermoFisher) was injected sub-cutaneously in the back of the C57BL6/J, *Cd74*$^{+/+}$ and *Cd74*$^{-/-}$ mice. 5, 10, 15 or 20 minutes post-injection, the mice were

killed and the skin at the site of injection was collected. Non-injected skin was used as a negative control for Dextran uptake. Skin was cut in small pieces and digested overnight in 2mL of liberase (0.25 mg/mL, from Sigma, in RPMI, HEPES (20µM) and Sodium Pyruvate (1 mM)), at 4°C, on a rotating wheel. Digested skins were homogenized by flushing up and down using a syringe equipped with an 18G needle. MHC II (I-A/I-E) (M5/114.15.2) Brilliant Violet 510 (107635, Biolegend), CD11c (N418) PE (phycoerythrin)-Cyanine7 (eBioscience), CD45 (30-F11) PE-Cyanine5.5 (eBioscience), EpCAM (epithelial cell adhesion molecule) (G8.8) APC (Allophycocyanin)-Cyanine7 (BioLegend) were purchased from Biolegend and eBioscence). Cells were stained on ice for 30 min in PBS with 0.5% BSA and EDTA (2 mM). Before acquisition, cells were washed three times and resuspended in PBS with 0.5% BSA and EDTA (2 mM). Fluorescence was then acquired on the LSRII (BD biosciences).

Intravital 2P imaging of the ear dermis

Two-photon intravital imaging of the ear dermis was performed as previously described (Filipe-Santos et al., 2009). In brief, mice were anesthetized and placed on a custom-designed heated stage and a coverslip sealed to a surrounding parafilm blanket was placed on the ear, to immerge a heated 25X/1.05 NA dipping objective (Olympus). Imaging was performed using an upright FVMPE-RS microscope (Olympus). Multiphoton excitation was provided by an Insight DS + Dual laser (Spectra-Physics) tuned at 950 nm. Emitted fluorescence was split with 520, 562 and 506 nm dichroic mirrors and passed through 593/40 (mTom if present) and 542/27 (YFP) filters to nondescanned detectors (Olympus) and 483/32 (collagen by second harmonic generation) and 520/35 (GFP) filters to GASP detectors (Olympus). Typically, images from about 10 z planes, spaced 4 µm were collected every minute for up to one hour. Edema was induced by subcutaneous injection of 10 µL of λ-carrageenan (from Sigma, 1% in saline). Imaging was performed 2 h after injection, around the site of injection.

QUANTIFICATION AND STATISTICAL ANALYSIS

In vitro migration experiments

Image processing and analysis was performed using Fiji software (Schindelin et al., 2012).

Analysis of channel filling

Profiles of Lucifer-Yellow, Dextran-AF647 and LifeAct-GFP were obtained along a central line on the microchannels using Fiji's Plot Profile function.

Cell bias toward low HR path

Only cells entering bifurcations devoid of any other cells were taken into account. Then, cells choosing the low resistance (or left) side of bifurcations (N_{LR}) and the ones choosing the high resistance (or right) side of bifurcations (N_{HR}) were counted manually. Bias was graphed as $(N_{LR} - N_{HR})/(N_{LR} + N_{HR})$, so that a bias of 0 corresponds to 50% of cells choosing each side, and a bias of 1 corresponds to 100% of cells choosing low resistance (or left) side. Error bars correspond to SEM. To determine significant bias toward low resistance path in each condition, we defined choice of low resistance path as "success", and we compared the number of successes to the hypothetical probability of 0.5 (corresponding to no bias) using a binomial test (one-tail p value: chance to observe more successes than the hypothetical probability of 0.5). Difference between conditions was determined by a Fisher exact test comparing the number of cells choosing each path for each condition (one-tailed if the outcome was predicted, two-tailed if it was not, *see* figure legends for detailed statistical analysis of each experiment).

Cell speed

Cell speed was analyzed using the manual tracking plugin of Fiji for images acquired in transmitted light or by automated tracking after segmentation using an homemade macro for fluorescent cells (LifeAct-GFP). Statistical difference between two conditions was determined by Mann-Whitney non-parametric t-test, or one-way ANOVA followed by a Tukey multicomparison test if more than 2 conditions were compared.

Actomyosin distribution and polarity

Actin and Myosin density maps generation was performed via a routine developed in the laboratory, as described in (Vargas et al., 2016). Individual migrating cells were segmented using automatic threshold (Triangle method) applied on the Lifeact-GFP signal or on the Myosin II-GFP signal. All time points of the same migrating cell were then cropped, normalized (in size and intensity) and averaged according to their migration direction. We thus obtained an image of the mean localization pattern of actin or myosin in the cell of interest. Mean images obtained for each cell were then normalized and averaged for each condition. Actin/Myosin-II profiles were obtained using the Plot Profile function. For each mean cell, we also computed a polarity index calculated as the difference of actin at the rear half and the front half of the cells normalized to the total cell actin (See **Fig. 3C**). To separate the cells in 3 polarity categories, we ordered the analyzed cells by increasing polarity indexes and separated them in 3 equal groups: category 1 regroups the third of the cells with the lowest polarity indexes, category 3 the third of the cells with the highest polarity indexes and category 2 the cells with intermediate polarity indexes. For polarity indexes, statistical differences between conditions were determined by a Mann-Whitney non-parametric t-test.

Actomyosin flow

Prior to analyze the retrograde flow, migrating cells were aligned over time using Fiji's multistackreg plugin. Kymographs showing Actin/Myosin-II retrograde flow were obtained

using a manually drawn line at the cell cortex to realize a montage. For Myosin-II flow maps and vector plots, we used Fiji's PIV (Particle Image Velocimetry) plugin (window size of 16 pixels (1.12 µm), correlation 0.6). To assess retrograde flow, we projected vectors along the X-axis, and averaged the different values for each x coordinate.

Cell shape and actomyosin in bifurcations

This analysis was achieved using an homemade macro. Briefly, movies of individual cells passing bifurcation were cropped and rotated according to their channel direction. For each movie, the bifurcation position was manually selected on the transmission channel and 3 regions of interest were defined: before bifurcation (area 1), losing arm side (area 2) and winning arm side (area 3). Then a mask of the migrating cell was obtained by thresholding on the GFP channel (LifeAct or Myosin-II), and Analyze Particles function was used to get the cell position and instantaneous velocity at each time point. Additionally, the area of cell mask was measure for each time point in the 3 regions of interest. We were thus able to define when the cell entered the bifurcation, when it chose the path to follow, and when it went out of the bifurcation. Time 0 (T_0) was defined as the time the cell entered the bifurcation (area 2 or area 3 >0). Retraction time (T_R) was defined as the first time point at which the losing arm was smaller than the previous time point (area 2 (T_R-1) > area 2 (T_R)). Passage time (T_{Pass}) was defined as the time the cell exited the bifurcations (area 1 and area 2 = 0). For averaging (see **Fig. S2**), cells were first aligned on T_0. Then, they were centered on retraction time. Finally they were normalized to the time of passage. "Centered time" is thus defined as (T-T_0)-T_R. "Normalized time" is defined as ((T-T_0)-T_R)/T_{Pass}. For arm length normalization, each arm area was divided by the average total area of the cell. For actomyosin ratio, statistics are calculated by a Wilcoxon test as the difference to the theoretical ratio of 1.

Macropinocytosis in microbifurcation analysis

Cell speed was quantified as described above. GFP images were auto-adjusted on Fiji. Then, cells were manually classified as positive for actin at the front if actin accumulation was visible (See Fig. S4) in front of the cell in at least one of the 4 time points (2 minutes) before the bifurcation (for before choice) or in at least one of the 6 time points (3 minutes) after the bifurcation (for after choice). Similarly, protrusion/retraction activity was quantified as at least one event of protrusion and retraction (See **Fig. S4**) in the 4 or 6 time points (2 or 3 minutes) before or after bifurcation respectively. For quantification of fluid uptake, the volume of dextran internalized by each cell was defined as the percentage of dextran intensity at the cell front when compared to extracellular dextran. We used the Lifeact-GFP signal to segment cell bodies and then defined the cell front as the 1/3 of the total cell body. Statistical difference between conditions was determined by Mann-Whitney non-parametric t-test.

Macropinosomes content release

To measure dextran release at the cell back during macropinocytosis, we realized kymographs of the side region of the cell, and measured dextran fluorescence signal in a rectangle region from the cortical actin to the exterior of the channel, to include all the space between the cell and the channel wall. We were able to visualize and measure variation of dextran intensities at the cell / channel interface at the cell rear after macropinosome resorption.

3D reconstruction of fluid passage

3D stacks of LifeAct-GFP migrating cells were acquired on the confocal microscope in presence of Dextran-AF647. A threshold was then performed on the Dextran channel to obtain a 3D mask. Extracellular dextran was separated from the intracellular dextran using LifeAct channel to delimit the cell. Intracellular dextran was further split between the front half and the rear half of the cell. 3D reconstructions were finally performed using Fiji's Volume Viewer plugin.

Exploration probability of bifurcations

To obtain the exploration probability of cells in bifurcations, we first obtained a mask of the explored area using a Z-projection (Max intensity) for 10 time points (corresponding to 5 min) of a segmented migrating cell (segmentation using auto-threshold, triangle method, on the LifeAct-GFP channel). Then, all the exploration masks were aligned on the bifurcation pattern and averaged for each condition. We thus obtained a mean exploration pattern of the bifurcations.

Macropinocytosis analysis by flow cytometry

In vitro assay

The results were analyzed with the FlowJo software (Tree Star, v10.1). iDCs were gated as $MHCII^+$ $CD115^-$. Fluid uptake was quantified by both the percentage of $ova488^+$ DCs as well as the ova488-MFI of DCs. Graphs represent the mean +/- sem of 3 replicates for one representative experiment, and the different conditions are compared to the control by a Mann-Whitney statistical test.

In vivo assay

Data were analyzed with FlowJo software (Tree Star, v10.1). Dead cells were excluded by using LIVE/DEAD™ Fixable Red Dead Cell Stain Kit (Invitrogen). Dermal DCs were identified as $CD45^+$ $CD11c^+$ $MHCII^+$ $EPCAM^-$ cells. Extracellular fluid uptake was quantified by both the percentage of Dextran-$AF647^+$ dermal DCs as well as the Dextran-AF647-MFI of $Dextran^+$ dermal DCs. Data are pooled from 2 independent experiments (represented by different symbols on the graphs), 3 mice per group, 2 injection sites per mouse (one on each flank). One dot represents the average value for one mouse. Conditions were compared using a 2-way ANOVA statistical test.

Intravital 2P imaging of the ear dermis analysis

Image processing and analysis was performed using Fiji software (Schindelin et al., 2012). Two-photon Zstack movies were first registered to correct the drift. Then, for the analysis, some "clean/transparent" volumes were chosen and cropped from those movies. Each cropped sub-movies were converted to RGB and Color Threshold function was apply to obtain a 3D mask of GFP cells or YFP cells. Hue was set to 0-44 for YFP and 45-255 for GFP and the brightness parameter was chosen for different depth in tissue and interpolated for the other Z planes. After obtaining 3D masks movies, we generated exploration masks: the 3D exploration mask at time n was define as the Max-projection of all 3D masks from time 0 to time n. We thus obtained a movie of the total seen volume by each cell population upon the time. By measuring this volume upon the time and normalizing it by the initial volume (total volume of GFP or YFP cells at time 0), we obtained a measurement indicating the ability to explore tissue for both cell types. Volume explored are plotted as $\Delta V/V_0 = (V-V_0)/V_0$. Exploration volume of *Cd74*$^{+/+}$ and *Cd74*$^{-/-}$ were compared using a two-way ANOVA test. Cells were tracked manually using Fiji's Manual Tracking plugin. Average cell velocity was graphed and statistical difference was evaluated by a Mann-Whitney non-parametric test.

Statistical analysis

The statistical tests, as well as number of cells per conditions (n) and number of experiments (N), are indicated in each description of analysis above and / or in each figure legends. All statistical analysis has been made with GraphPad Prism software (v6).

KEY RESOURCES TABLE

SUPPLEMENTAL INFORMATION

Movie S1: iDCs migrating microbifurcations, related to Figure 1. Symmetric ((R+ΔR)/R=1, left), weakly asymmetric ((R+Δ R)/R=5, middle) or strongly asymmetric (DE/1, right). Images acquired on a videomicroscope, 10X magnification, 1 image / 30 sec.

Movie S2: Myosin II flow analysis by PIV, related to Figure 2. Representative Myosin-II flow of a Myosin II-GFP iDC migrating in straight channels (before the bifurcation), analyzed by PIV. Top: Myosin II-GFP image. Bottom: PIV vectors. Direction of arrows indicates direction of movement for each particle analyzed, color of arrows indicates particle speed. Images acquired on a confocal microscope, 40X magnification, 1 image / 3 sec.

Movie S3, A small force imbalance amplified by the actomyosin network accounts for barotaxis related to Figure 2. A. Simulated cell (left) and iDC (right) migrating in symmetric bifurcations (00:02). Shape of cells were obtained by thresholding the actin (or LifeAct-GFP) signal to obtain the cell mask. **B. Actin distribution in simulated cell (left) and iDC (right) migrating in a symmetric bifurcation (00:04). C. Myosin distribution in an iDC migrating in a symmetric bifurcation (00:07).** All images acquired on a videomicroscope, 10X magnification, 1 image / 30 sec.

Movie S4, iDCs migrating in elevated hydraulic resistance paths (dead-ends) are macropinocytic, related to Figure 4. A. iDCs migrating in open- or dead-ends (00:02). Green: LifeAct. Red: Dextran-AF647. Images acquired on a videomicroscope, 20X magnification, 1 image / 30 sec. **B. 3D confocal reconstruction of an iDC migrating in a dead-end (00:06).** Top: original confocal image. Green: LifeAct-GFP, red: Dextran-AF647. Bottom: 3D-reconstruction. Grey: total dextran signal, red: external dextran (signal outside of the LifeAct-GFP mask), green: internal dextran (signal inside of the LifeAct-GFP mask). Images acquired on a confocal microscope, 40X magnification.

Movie S5, Macropinocytosis provides iDCs with a unique capacity to overcome barotaxis, related to Figure 5. A. iDCs migrating in small (~20 μm²) or large (~30 μm²) microchannels (00:02). Green: LifeAct. Red: Dextran-AF647. Images acquired on a videomicroscope, 20X magnification, 1 image / 30 sec. **B. iDCs migrating in large (~30 μm²) open- or dead-ends (00:06).** Green: LifeAct. Red: Dextran-AF647. Images acquired on a videomicroscope, 20X magnification, 1 image / 30 sec. **C. Fluid passage in small (~20 μm²) (00:10) or large (~30 μm²) (00:26) microchannels.** 3D-reconstruction and segmentation of Dextran-AF647. Top: original confocal image. Green: LifeAct-GFP, red: Dextran-AF647. Bottom: 3D-reconstruction. Grey: total dextran signal, red: external dextran (signal outside of the LifeAct-GFP mask), blue: rear internal dextran (signal inside of the rear half of the LifeAct-GFP mask, corresponding to lysosomes), green: front internal dextran (signal inside of the front half of the LifeAct-GFP mask, corresponding to macropinosomes). Images acquired on a confocal microscope, 40X magnification. **D. Release of macropinosomes during iDC migration (00:41).** Fluid pockets form between the cell and the channel wall after a macropinosome content is emptied in the extracellular space (highlighted by white arrows). The cell then deforms around the pocket to pursue its migration. Green: LifeAct. Red: Dextran-AF647. Images acquired on a confocal microscope, 20X magnification, 1 image / 10 sec. **E. Cell deforms around fluid pocket and let fluid flow to their rear (00:59).** iDC migrating in a large channel. The content of one macropinosome is released in the extracellular space. Note that after this event, the cell deforms its rear to let fluid pass (top) and that the fluorescence signal between the cell and the channel wall (bottom) increases, suggesting that fluid can then flow behind the cell. Images acquired on a confocal microscope, 20X magnification, 1 image / 3 sec.

Movie S6, Macropinocytic iDCs are more efficient at exploring their environment, related to Figure 6. A. Intravital imaging of CD11c-EYFP dermal DCs (00:01). Dermal

DCs extend and retracts protrusions when changing direction *in vivo*. Complete field of view with cell tracks (white), and zooms of 5 cells making directional choice in the tissue. Yellow spots indicate the losing arm during choice. **B. iDC migration on two-dimensional surfaces does not rely on arms extension and retraction (00:13).** Confocal imaging of LifeAct iDCs migrating on fibronectin coated glass. Inverted LUT, images acquired on a confocal microscope, 40X magnification, 1 image / min. **C. Space exploration by iDCs migrating after local edema induction in the ear dermis (00:20).** Magenta: *Cd74*$^{+/+}$ cells. Cyan: *Cd74*$^{-/-}$ cells. Yellow outline: cumulated space explored. All images acquired on a two-photon microscope, 25X magnification, 1 image / 30-50 sec.

Data S1: Physical description of dendritic cell migration at bifurcations, related to STAR methods. I. Amoeboid-like migration in channels. II. Generalization of the dynamics at the intersection point. III. Classification of the asymptotic states. IV. Cell interface kinematic equations. V. Qualitative description of the dynamics at bifurcations. VI. Cell bias in dead-end bifurcations. VII. Effects of contractility / permeability on the dynamics after retraction. VIII. Statistics of model cells in random mazes.

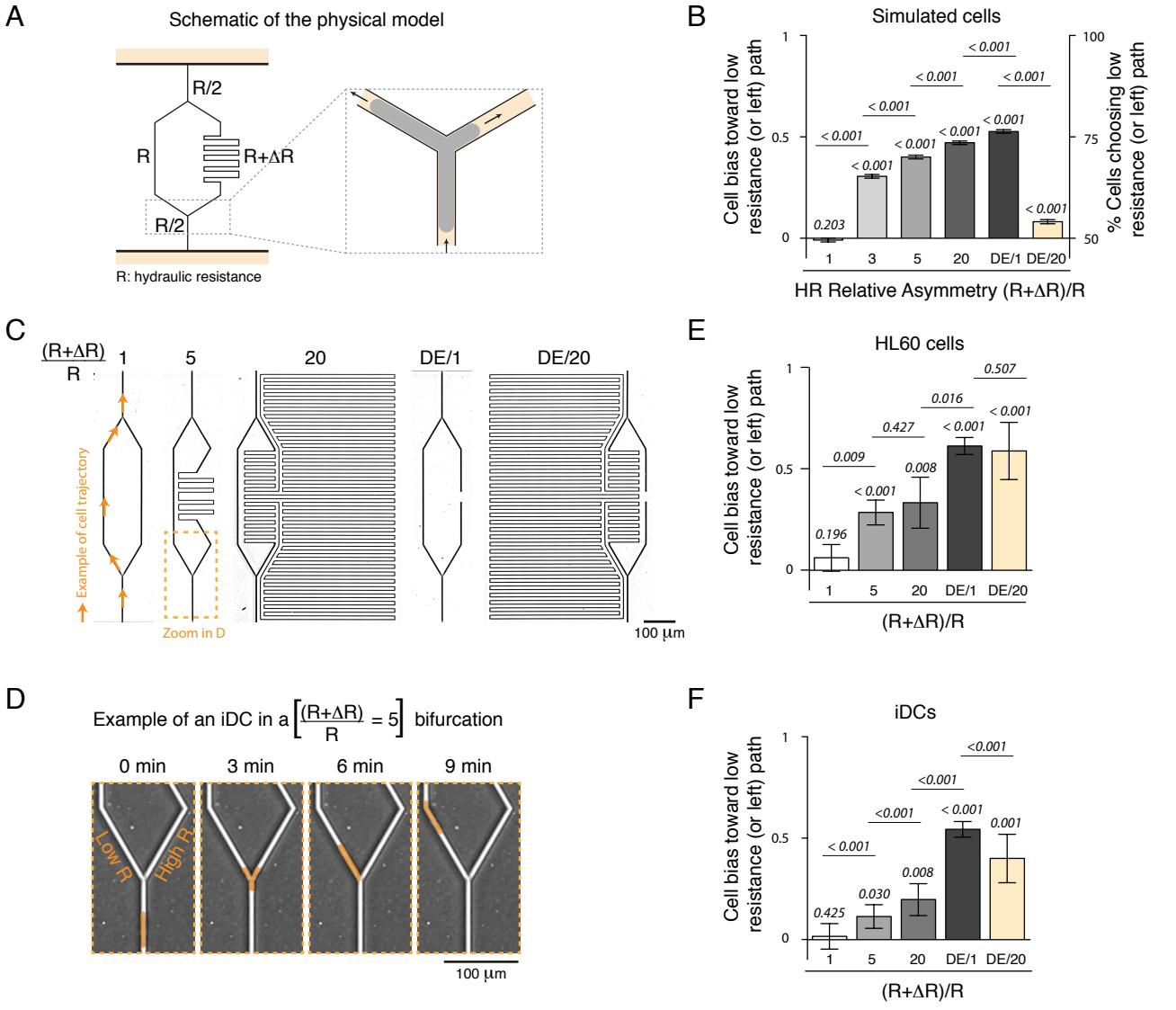
A
Schematic of the physical model
R/2
R
R+ΔR
R/2
R: hydraulic resistance
B
Simulated cells
Cell bias toward low resistance (or left) path
% Cells choosing low resistance (or left) path
HR Relative Asymmetry (R+ΔR)/R
1
3
5
20
DE/1
DE/20
0.203
< 0.001
C
(R+ΔR)/R
Example of cell trajectory
Zoom in D
100 µm
E
HL60 cells
Cell bias toward low resistance (or left) path
(R+ΔR)/R
0.196
0.009
< 0.001
0.427
0.008
0.016
< 0.001
0.507
< 0.001
D
Example of an iDC in a [(R+ΔR)/R = 5] bifurcation
0 min
3 min
6 min
9 min
Low R
High R
100 µm
F
iDCs
Cell bias toward low resistance (or left) path
(R+ΔR)/R
0.425
< 0.001
0.030
<0.001
0.008
<0.001
< 0.001
<0.001
0.001

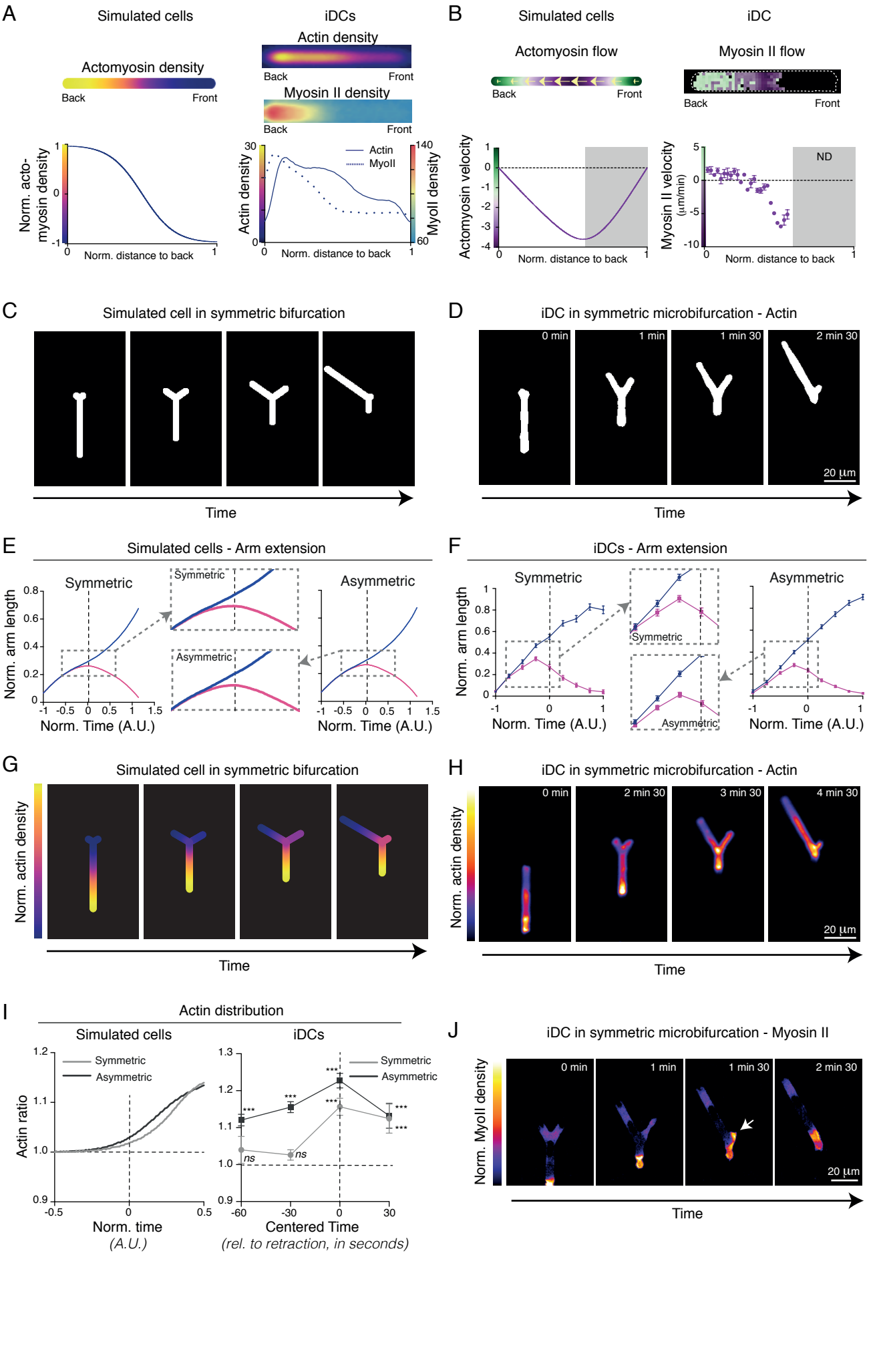
A
Simulated cells
iDCs
Actomyosin density
Back
Front
Actin density
Myosin II density
Norm. acto-myosin density
Norm. distance to back
Actin density
MyoII density
Actin
MyoII
B
Simulated cells
iDC
Actomyosin flow
Myosin II flow
Actomyosin velocity
Myosin II velocity (µm/min)
ND
C
Simulated cell in symmetric bifurcation
Time
D
iDC in symmetric microbifurcation - Actin
0 min
1 min
1 min 30
2 min 30
20 µm
E
Simulated cells - Arm extension
Symmetric
Asymmetric
Norm. arm length
Norm. Time (A.U.)
F
iDCs - Arm extension
G
Simulated cell in symmetric bifurcation
Norm. actin density
H
iDC in symmetric microbifurcation - Actin
3 min 30
4 min 30
I
Actin distribution
Simulated cells
iDCs
Actin ratio
Norm. time (A.U.)
Centered Time (rel. to retraction, in seconds)
ns
J
iDC in symmetric microbifurcation - Myosin II
Norm. MyoII density

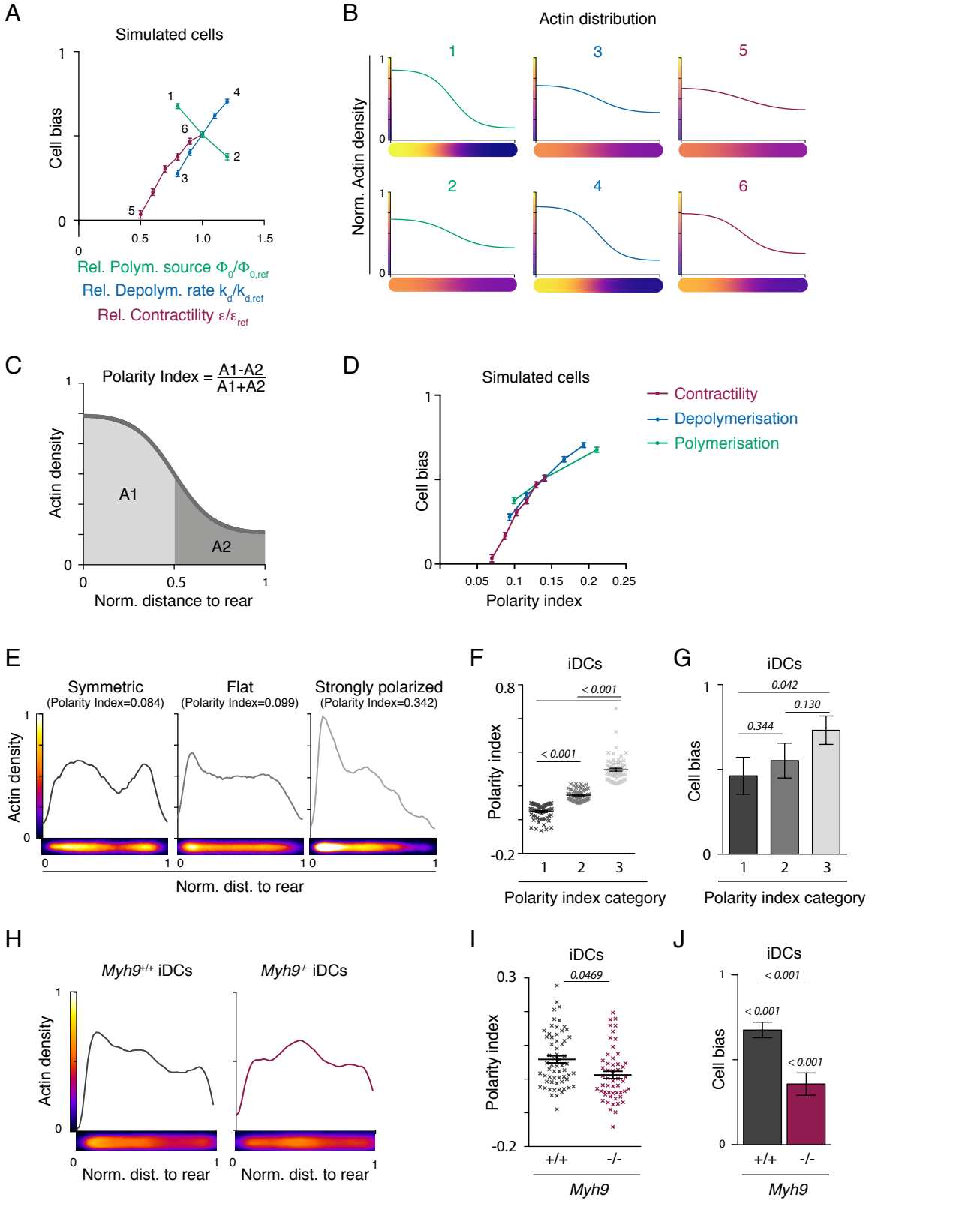
A
Simulated cells
Cell bias
Rel. Polym. source $\Phi_0/\Phi_{0,ref}$
Rel. Depolym. rate $k_d/k_{d,ref}$
Rel. Contractility $\varepsilon/\varepsilon_{ref}$
B
Actin distribution
Norm. Actin density
C
Polarity Index = A1-A2 / A1+A2
Actin density
A1
A2
Norm. distance to rear
D
Simulated cells
Contractility
Depolymerisation
Polymerisation
Cell bias
Polarity index
E
Symmetric
(Polarity Index=0.084)
Flat
(Polarity Index=0.099)
Strongly polarized
(Polarity Index=0.342)
Actin density
Norm. dist. to rear
F
iDCs
Polarity index
< 0.001
< 0.001
Polarity index category
G
iDCs
Cell bias
0.042
0.130
0.344
Polarity index category
H
Myh9+/+ iDCs
Myh9-/- iDCs
Actin density
Norm. dist. to rear
Norm. dist. to rear
I
iDCs
Polarity index
0.0469
+/+
-/-
Myh9
J
iDCs
Cell bias
< 0.001
< 0.001
< 0.001
+/+
-/-
Myh9

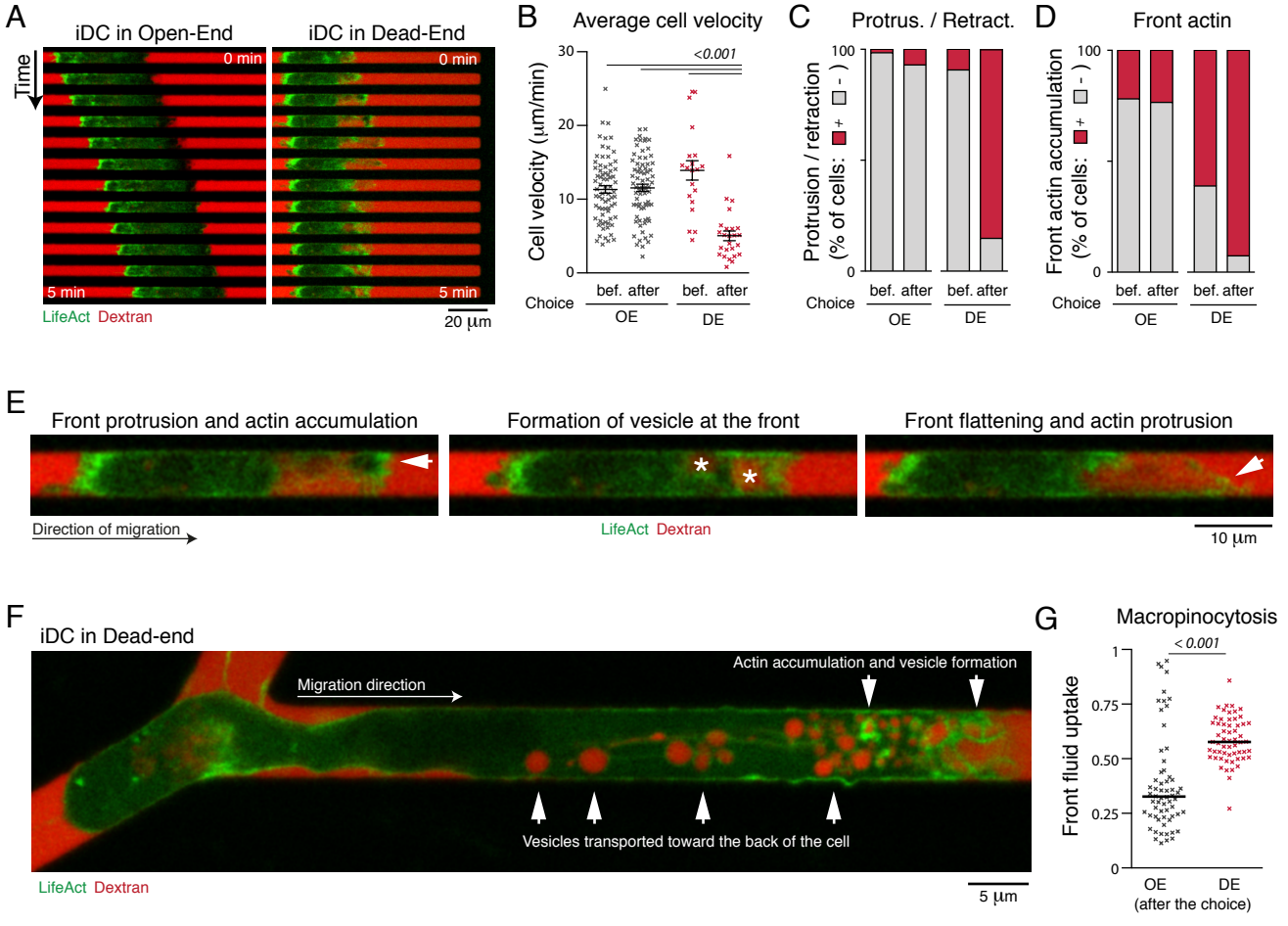
A
iDC in Open-End
iDC in Dead-End
Time
0 min
0 min
5 min
5 min
LifeAct Dextran
20 µm
B
Average cell velocity
<0.001
Cell velocity (µm/min)
30
20
10
0
Choice
bef. after
bef. after
OE
DE
C
Protrus. / Retract.
Protrusion / retraction (% of cells: + -)
100
0
Choice
bef. after
bef. after
OE
DE
D
Front actin
Front actin accumulation (% of cells: + -)
100
0
Choice
bef. after
bef. after
OE
DE
E
Front protrusion and actin accumulation
Formation of vesicle at the front
Front flattening and actin protrusion
Direction of migration
LifeAct Dextran
10 µm
F
iDC in Dead-end
Migration direction
Actin accumulation and vesicle formation
Vesicles transported toward the back of the cell
LifeAct Dextran
5 µm
G
Macropinocytosis
< 0.001
Front fluid uptake
1
0.75
0.50
0.25
0
OE
DE
(after the choice)

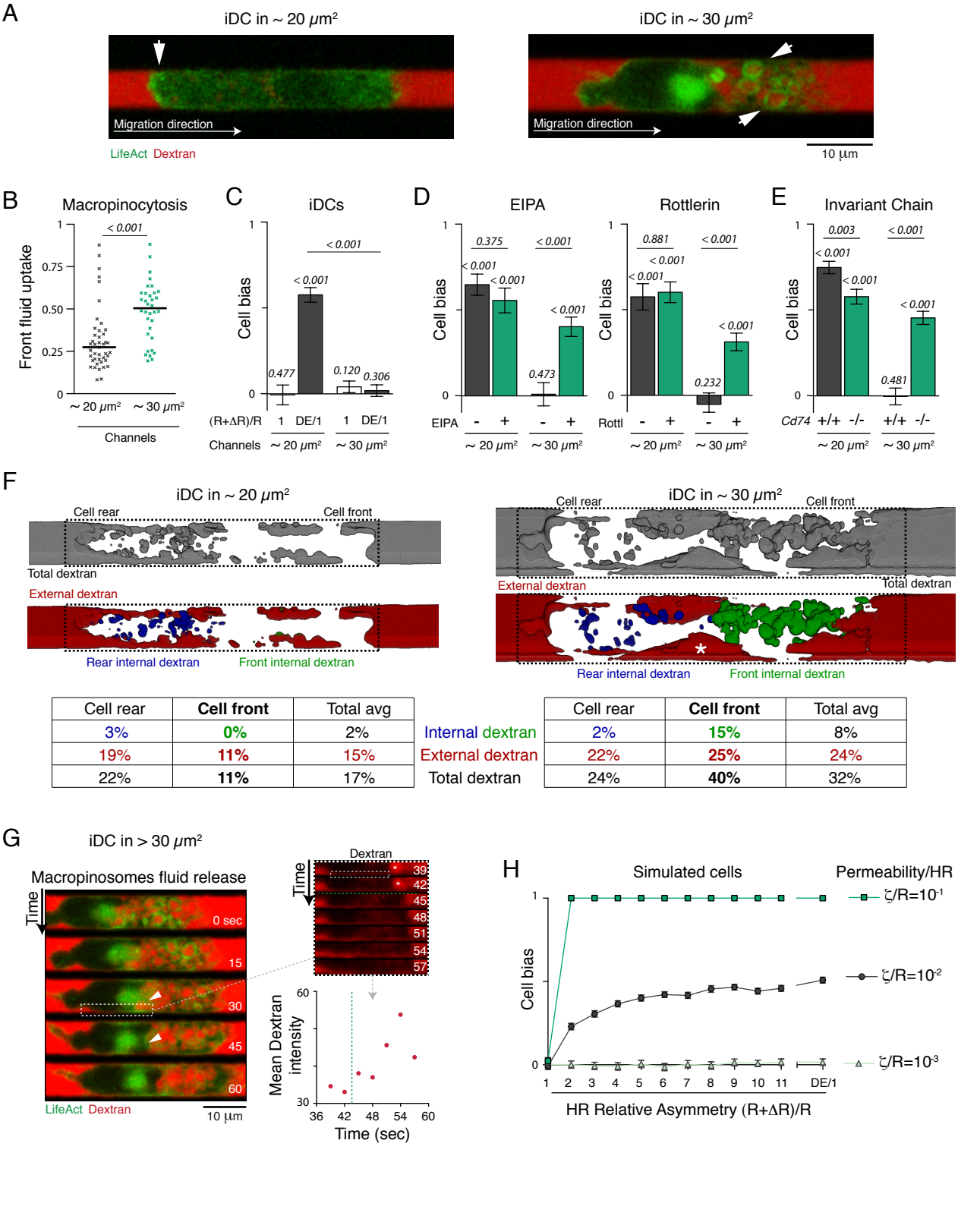

Cell rear	**Cell front**	Total avg
3%	**0%**	2%
19%	**11%**	15%
22%	**11%**	17%

	Cell rear	**Cell front**	Total avg
Internal dextran	2%	**15%**	8%
External dextran	22%	**25%**	24%
Total dextran	24%	**40%**	32%

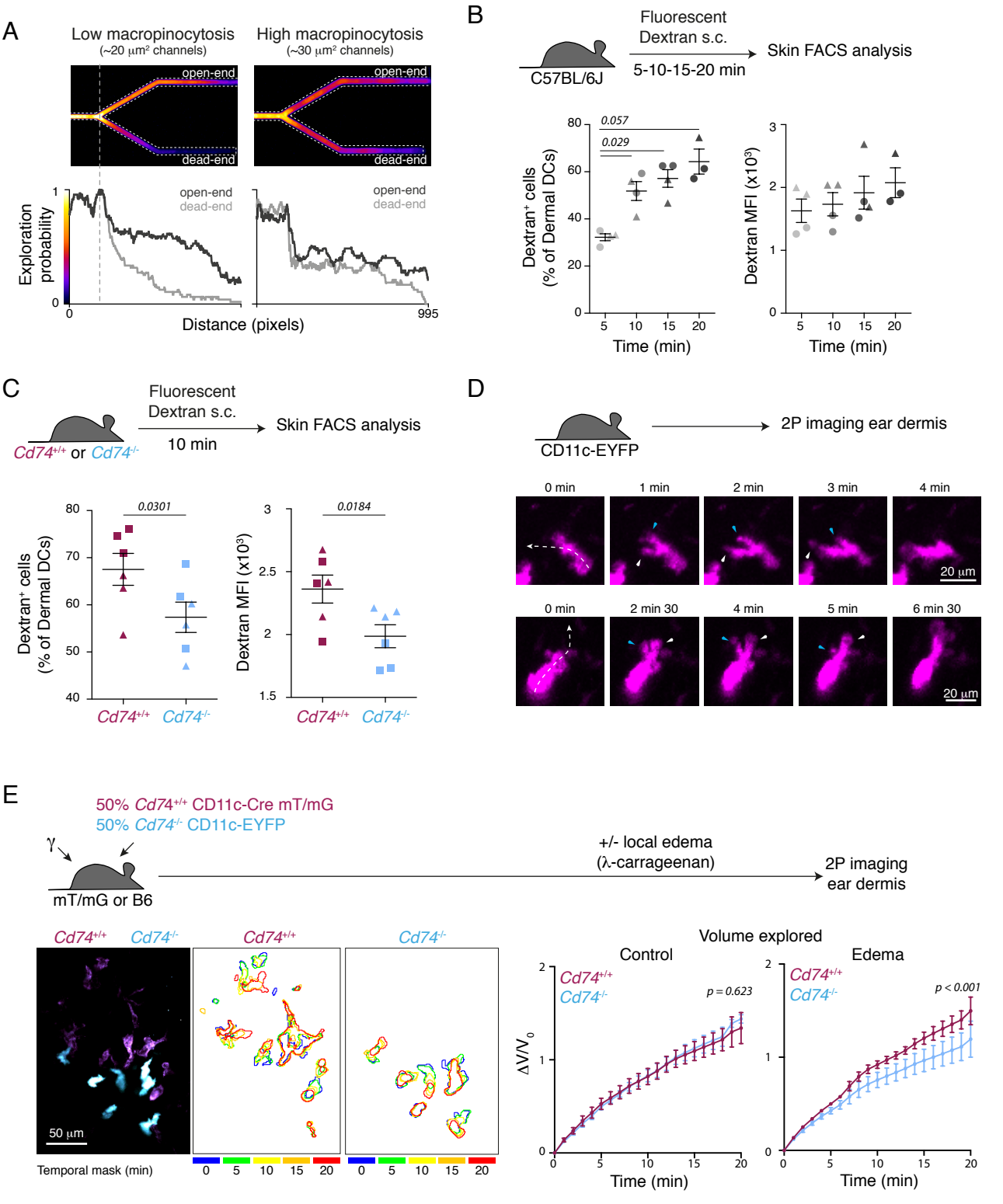
A
Low macropinocytosis
(~20 μm² channels)
High macropinocytosis
(~30 μm² channels)
open-end
dead-end
Exploration probability
Distance (pixels)
B
C57BL/6J
Fluorescent Dextran s.c.
5-10-15-20 min
Skin FACS analysis
Dextran⁺ cells (% of Dermal DCs)
Dextran MFI (x10³)
Time (min)
0.057
0.029
C
Cd74+/+ or Cd74-/-
Fluorescent Dextran s.c.
10 min
Skin FACS analysis
0.0301
0.0184
D
CD11c-EYFP
2P imaging ear dermis
0 min
1 min
2 min
3 min
4 min
2 min 30
5 min
6 min 30
20 μm
E
50% Cd74+/+ CD11c-Cre mT/mG
50% Cd74-/- CD11c-EYFP
mT/mG or B6
+/- local edema
(λ-carrageenan)
2P imaging
ear dermis
50 μm
Temporal mask (min)
Volume explored
Control
Edema
ΔV/V0
p = 0.623
p < 0.001

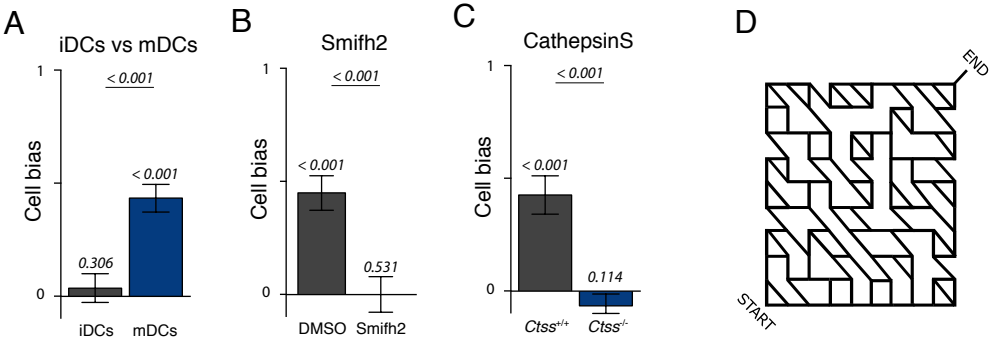
A
iDCs vs mDCs
Cell bias
1
0
< 0.001
< 0.001
0.306
iDCs
mDCs
B
Smifh2
Cell bias
< 0.001
< 0.001
0.531
DMSO
Smifh2
C
CathepsinS
Cell bias
< 0.001
< 0.001
0.114
Ctss+/+
Ctss-/-
D
END
START

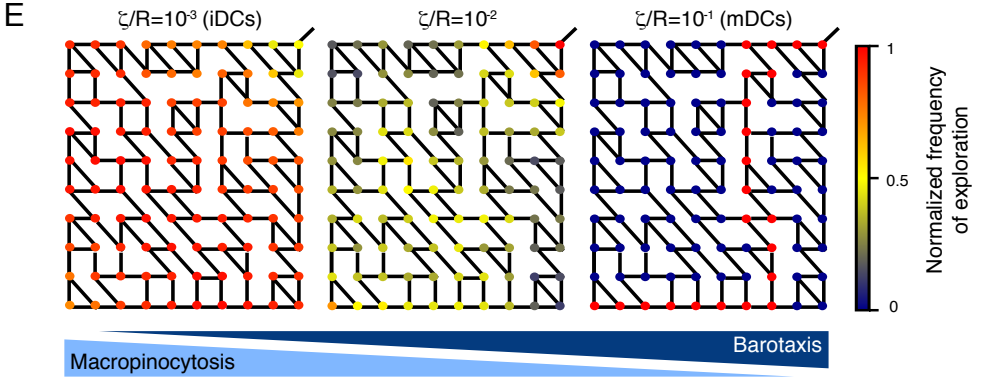
E
ζ/R=10-3 (iDCs)
ζ/R=10-2
ζ/R=10-1 (mDCs)
1
0.5
0
Normalized frequency of exploration
Barotaxis
Macropinocytosis

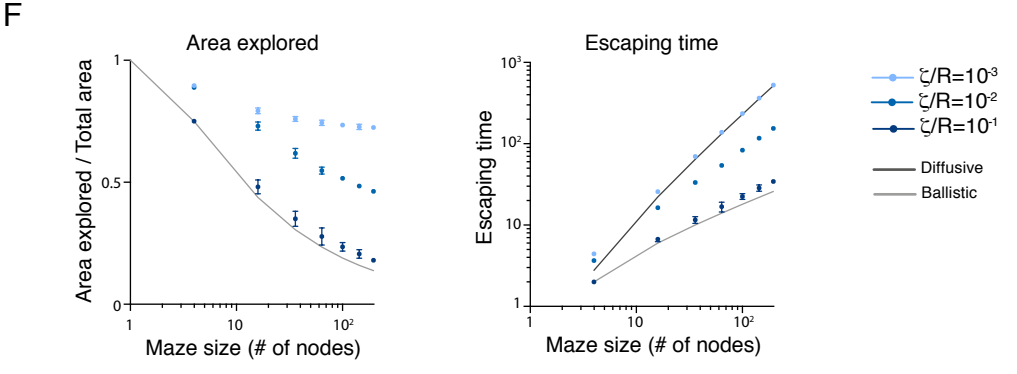
F
Area explored
Area explored / Total area
1
0.5
0
1
10
10²
Maze size (# of nodes)
Escaping time
Escaping time
10³
10²
10
1
1
10
10²
Maze size (# of nodes)
ζ/R=10-3
ζ/R=10-2
ζ/R=10-1
Diffusive
Ballistic

Dendritic cell patrolling in the skin

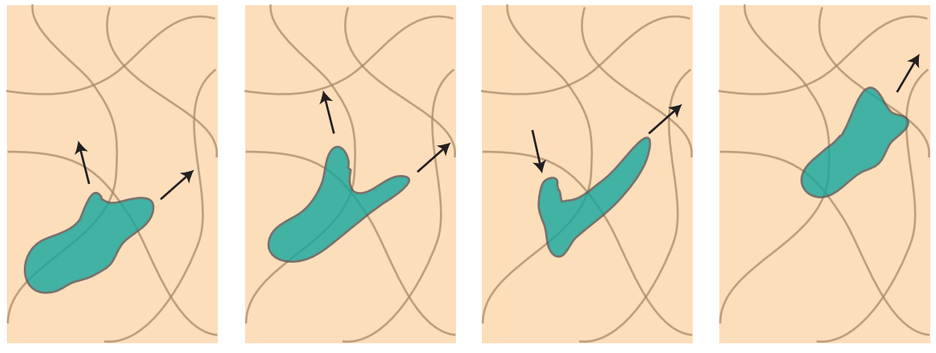

Time

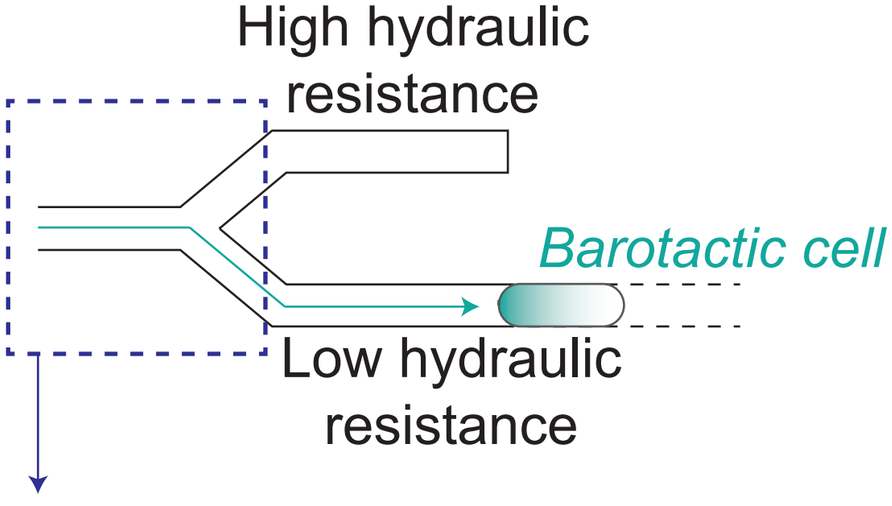

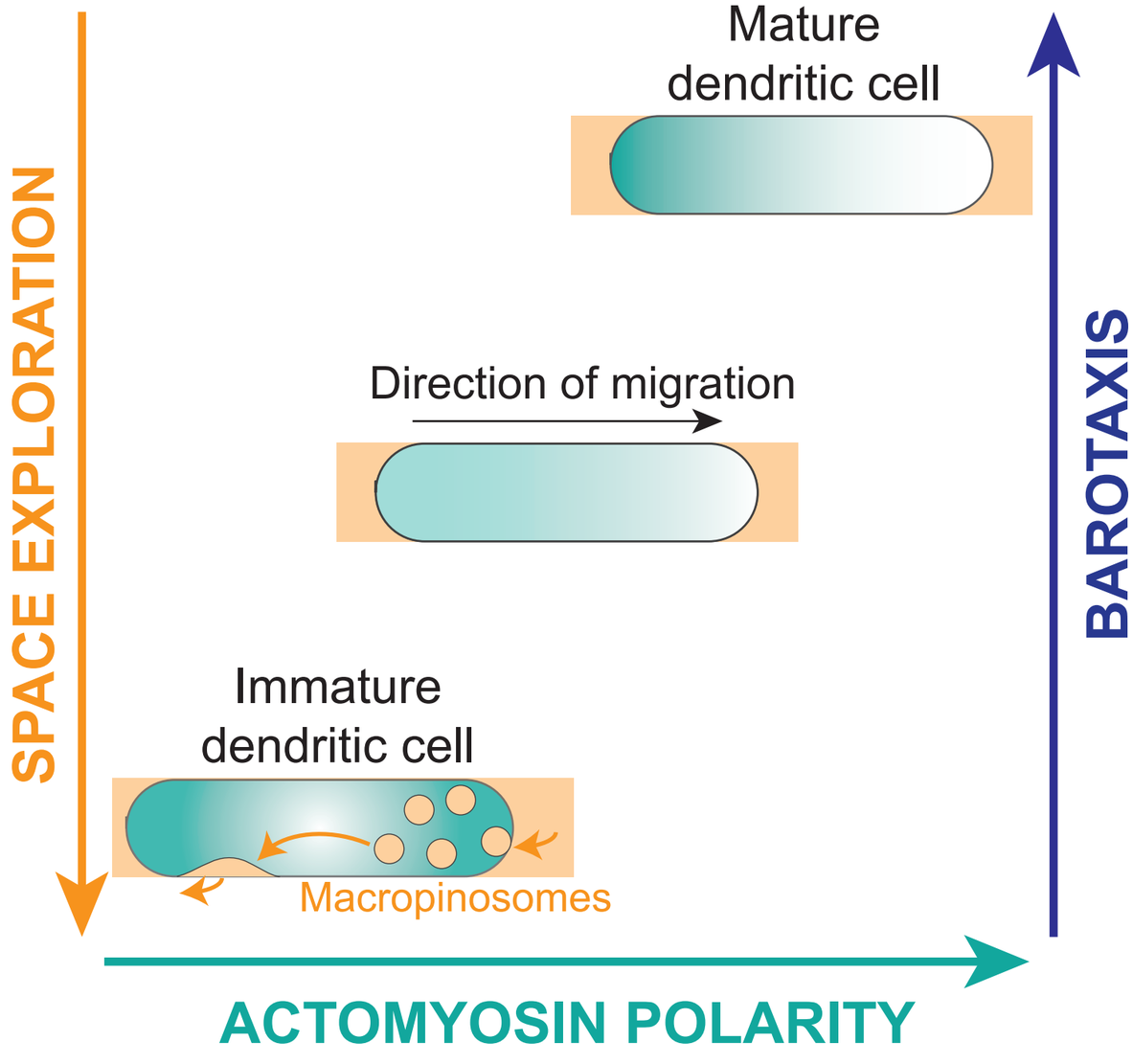

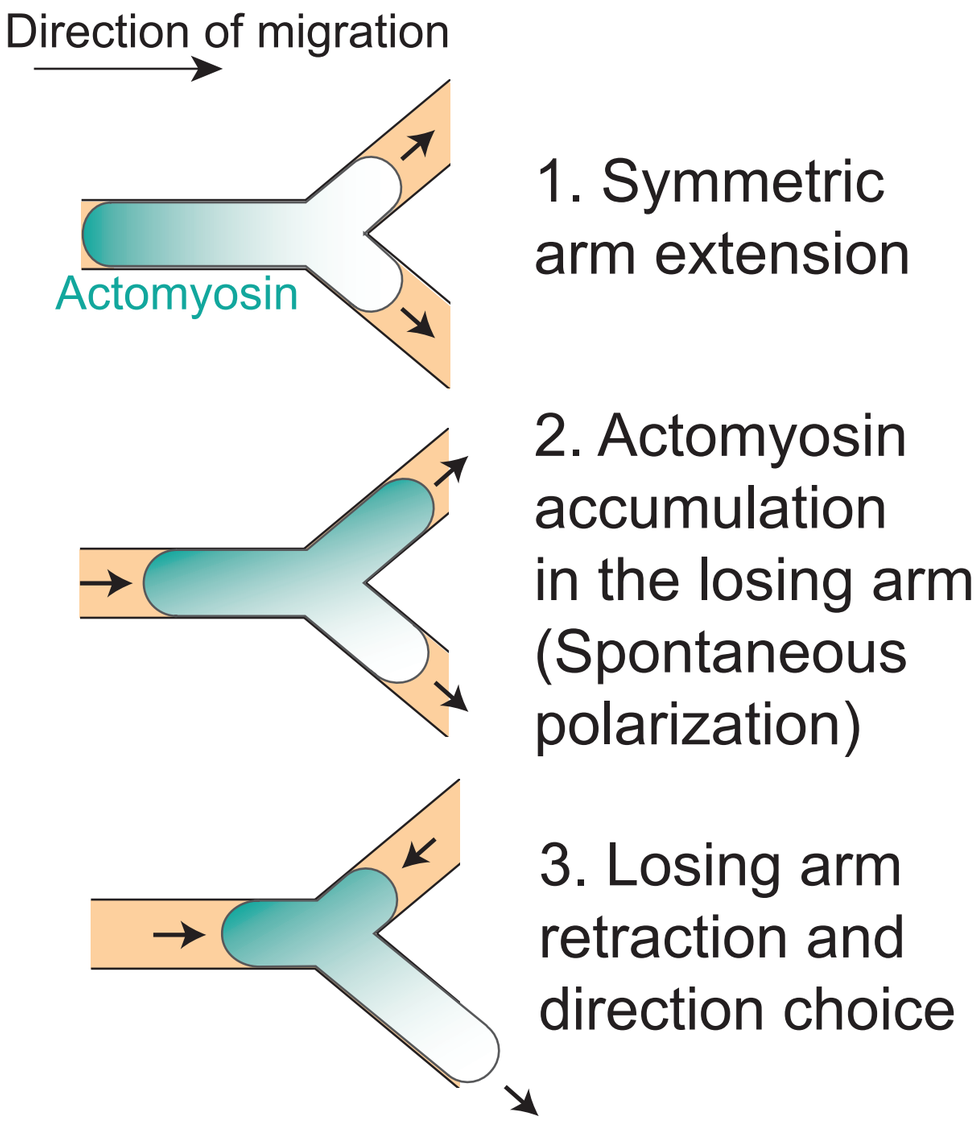

Macropinocytic dendritic cell:
exhaustive space exploration

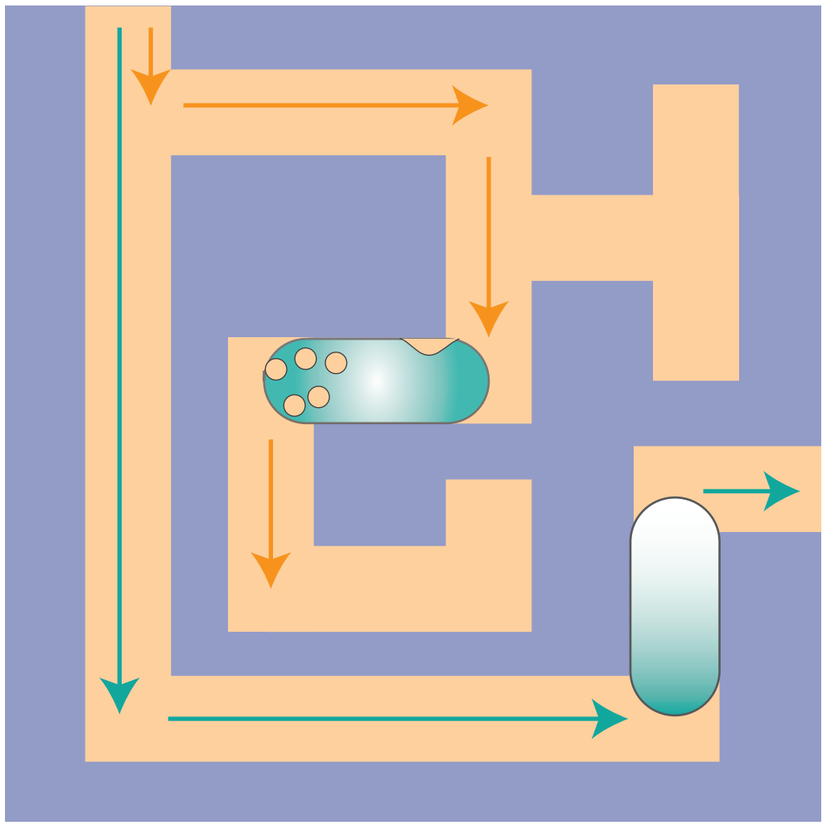

Barotactic dendritic cell:
shortest path